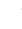



Hyper-massive Black Holes have Faint Broad and Narrow Emission Lines

Harshitha K. Bhat^{1,2,3} , Susmita Chakravorty⁴ , Dhrubojyoti Sengupta⁵,
Martin Elvis⁶, Sudeb Ranjan Datta⁴, Nirupam Roy⁴, Caroline Bertemes⁷,
Gary Ferland⁸, Savithri H. Ezhikode⁹

¹Department of Physics, St. Joseph's College, 36 Lalbagh Road, Bangalore 560027, India

²I. Physikalisches Institut der Universität zu Köln, Zùlpicher Str. 77, 50937 Köln, Germany

³Max-Planck-Institut für Radioastronomie, Auf dem Hügel 69, 53121 Bonn, Germany

⁴Department of Physics, Indian Institute of Science, Bangalore 560012, India; write2susmita@gmail.com

⁵Presidency University, 86/1 College Street, Kolkata 700073, India

⁶Harvard-Smithsonian Center for Astrophysics, 60 Garden Street, Cambridge, MA 02138, USA

⁷Department of Physics, University of Bath, Claverton Down, Bath BA2 7AY, UK

⁸Department of Physics and Astronomy, University of Kentucky, Lexington, KY 40506, USA

⁹Inter-University Centre for Astronomy & Astrophysics (IUCAA), Ganeshkhind, Pune, India

9 April 2024

ABSTRACT

The EUV provides most of the ionization that creates the high equivalent width (EW) broad and narrow emission lines (BELs, NELs) of quasars. Spectra of Hypermassive Schwarzschild black holes (HMBHs, $M_{BH} \geq 10^{10} M_{\odot}$) with α -discs, decline rapidly in the EUV suggesting much lower EWs. Model spectra for black holes of mass $10^6 - 10^{12} M_{\odot}$ and accretion rates $0.03 \leq L_{bol}/L_{edd} \leq 1.0$ were input to the CLOUDY photoionization code. BELs become ~ 100 times weaker in EW from $M_{BH} \sim 10^8 M_{\odot}$ to $M_{BH} \sim 10^{10} M_{\odot}$. The high ionization BELs (O VI 1034 Å, C IV 1549 Å, He II 1640 Å) decline in EW from ($M_{BH} \geq 10^6 M_{\odot}$, reproducing the Baldwin effect, but regain EW for $M_{BH} \geq 10^{10} M_{\odot}$). The low ionization lines (MgII 2798 Å, H β 4861 Å and H α 6563 Å) remain weak. Lines for maximally spinning HMBHs behave similarly. Line ratio diagrams for the BELs show that high OVI/H β and low CIV/H α may pick out HMBH, although OVI is often hard to observe. In NEL BPT diagrams HMBHs lie among star forming regions, except for highly spinning, high accretion rate HMBHs. In summary, the BELs expected from HMBHs would be hard to detect using the current optical facilities. From 10^6 to $10^{12} M_{\odot}$, the emission lines used to detect AGN only have high EW in the $10^6 - 10^9 M_{\odot}$ window, where most AGN are found. This selection effect may be distorting reported distributions of M_{BH} .

Key words: Galaxies - active, quasars: emission lines, quasars: supermassive black holes, Physical Data and Processes - accretion, accretion discs, black hole physics, line: formation

1 INTRODUCTION

Active galactic nuclei (AGN) are the central regions of galaxies that host Super-massive black holes (SMBHs) which are actively accreting surrounding material. They have been an exciting field of research in Astrophysics for along time now

(Netzer 2015, and references therein). The gravitational potential energy of the infalling matter is converted into radiation which photoionizes both the unresolvable nearby ($\lesssim 0.1$ pc, to the black hole) and more distant ($\lesssim 100$ pc, partially resolvable in near AGN) gas which then re-emit as Broad and Narrow Emission Lines (BELs & NELs) respectively, in the optical and UV regions. The NELs usually have Doppler widths ≤ 500 km s⁻¹ and arise in relatively low density ($\sim 10^3$ cm⁻³) gas. BELs have Doppler widths

* E-mail: harshikikkeri@gmail.com (HB)

† Email: write2susmita@gmail.com (SC)

$\sim 1,000 - 10,000 \text{ km s}^{-1}$ and arise in higher density gas ($\sim 10^9 \text{ cm}^{-3}$) as determined by absence of certain forbidden lines. Such large Doppler widths in the BELs suggest that the broad line regions (BLRs) are in deep gravitational potential where Keplerian velocities are often $> 1\%$ c , which makes BELs very important in understanding the central source. Furthermore, the presence of BELs is an indicator of AGN activity.

Studying the BELs & NELs in AGN and using them to understand fundamental properties, particularly the mass, of the associated black holes (BHs) is a well-established method. New data from more and more sensitive multi-wavelength campaigns suggest the presence of Hyper-massive Black Holes (HMBHs) ($M_{BH} \geq 10^{10} M_{\odot}$) which are extreme and/or unusual for AGN (Fan et al. 2001; Mortlock et al. 2011; Wu et al. 2015, e.g. []). King (2015) gives a maximum theoretical limit for M_{BH} through luminous accretion as $\sim 5 \times 10^{10} M_{\odot}$ for typical parameters. Of the $> 10^5$ quasars known only a few tens have black hole masses $> 10^{10} M_{\odot}$ (Natarajan & Treister 2009; Ichikawa & Inayoshi 2017). This scarcity may be because they are rare, or perhaps cannot grow any larger. Discovery of more HMBH will put serious constraints on the current models for seed black holes. (Volonteri 2012; Johnson et al. 2013; Natarajan 2014; Latif & Ferrara 2016). Finding even one black hole with $M_{BH} \geq 10^{11} M_{\odot}$ at high redshift ($z > 6$) would pose serious challenges for the existing black hole evolution theories, requiring either highly super-Eddington accretion or super-massive seed black holes.

Here we investigate whether this paucity of HMBH could be a selection effect due to the cooler temperatures of alpha-disc accretion discs at high masses. We were motivated by the striking results for low mass ($< 10^5 M_{\odot}$) BHs by Chakravorty et al. (2014), who found that BLR emission is drastically (factor > 10 for $H\beta$ 4861 Å) and quite suddenly (in < 1 dex in mass from 10^5 to $10^4 M_{\odot}$) reduced as the discs become too hot and overionize gas moving at Keplerian speeds $> 1000 \text{ km/s}$. A complementary effect is expected as the discs become too cool (in case of HMBHs) to photoionize the gas to produce the typical BLR emission lines. That cooler accretion discs would result in weaker line emission, was first investigated analytically by (Laor & Davis 2011). Hence we can expect that the emission lines will be weaker for HMBHs. Here we make a detailed investigation of the predicted BLR and NLR equivalent widths (EWs) as a function of HMBH mass.

As the mass estimates for AGN come from the detection of broad emission lines in the UV and optical region of the AGN spectra, we wanted to know if the same methods of detection are possible for HMBH. Therefore, we investigate the predicted EWs of few prominent BELs over a wide range of black hole masses ($M_{BH} = 10^6 - 10^{12} M_{\odot}$) and accretion rates ($L_{bol}/L_{edd} = 0.03 - 1$), to see if there is a decrease in intrinsic line strengths among these BELs, making such BHs very hard to be discovered with our current standard detection methods. See section 5.

The strengths of the BELs and NELs depend on the ionizing spectral energy distribution (SED), which in turn depends on the fundamental properties of the BH: its mass and the rate at which it is accreting matter. Larger BHs have cooler maximum temperatures. At some mass the ionizing photons they emit will drop, potentially weakening their

BELs and NELs to the point of undetectability. Investigating whether this happens for HMBHs is the purpose of this paper. The mass accretion rate (\dot{m}) can be related to the ratio between the bolometric luminosity (L_{bol}) of the accretion disc of accreted matter around the black hole, to the classical Eddington luminosity L_{edd} of the BH. In Section 2 we shall show the details of how we have related the accretion rate with L_{bol}/L_{edd} . Thus, throughout the paper, the accretion rate will be represented by L_{bol}/L_{edd} .

Since we are interested in the higher end of the BH masses, we could not rely on the conventional method of assuming broken power-laws to construct the broad band SEDs of the BHs (Tananbaum et al. 1979; Lusso & Risaliti 2016). In section 2, we elaborate on the methods adopted to properly link the different components of the AGN SED, while being careful about the mass evolution of these inter-relations.

Unlike BELs, NELs are not necessarily signatures of AGN activity. Dynamically (velocity widths), NELs are very similar to the emission lines of star-forming regions, planetary nebulae and even supernova remnants, as the photoionization equilibrium in all these regions is achieved at around same temperatures ($T \sim 10^4 \text{ K}$). To distinguish between narrow emission lines from all these different astrophysical objects, BPT diagrams (Baldwin, Phillips & Terlevich 1981) were made as an attempt to have diagnostic diagrams for NELs in SMBH. Using our predicted strengths of NELs we also investigate the line ratios of HMBHs on BPT diagrams. See section 6. Since the BPT diagrams are well-tested tools to find NELs, in AGN, we extend the same logic to look at BELs. Since now we are looking at a much wider range of physical parameters of the black holes, we do not expect the broad lines to show intensity variations within a standard small range, anymore. See section 7.2 for the interesting consequences of mass and accretion rate variation on the line ratios of different BELs.

In this study, we have used the photoionization code called CLOUDY¹ (Ferland et al. 2017), to predict the emission line strengths as a function of M_{BH} and L_{bol}/L_{edd} . The physical parameters used for the CLOUDY calculations are mentioned in detail in Section 3. To model the gas/clouds that produce the BELs and NELs, we use the “locally optimally emitting cloud (LOC)” model (Baldwin et al. 1995), which suggests that the emission lines are produced optimally - that each line is produced most efficiently within a narrow range of density and incident light flux. The history of this model and how we use it in this paper have been detailed in Section 4.

2 SPECTRAL ENERGY DISTRIBUTION

2.1 The radiation from the accretion disc

The main source of energy in AGN is the conversion of gravitational potential energy of the accreting matter into radiation. This radiation from the accretion disc around the black hole, peaks in the extreme-ultraviolet region (EUV, 10-100eV). The SED of AGN is broad band, extending from radio wavelengths to gamma rays. However, for the study of

¹ <http://www.nublado.org/>

photoionized gas, the range from optical-UV to soft X-rays matters most, because these photons ionize the gas present in the central ~ 100 pc of the AGN. Observationally there is uncertainty in the shape of the SED of the radiation from the accretion disc near its peak, due to absorption of EUV radiation by Galactic neutral gas and dust. Therefore, observations below 10 eV and above 100 eV have to be used to reconstruct the unobserved part of SEDs.

According to standard theory of accretion discs (Shakura & Sunyaev 1973; Frank, King & Raine 2002), radiation from the accretion disc can be modeled as the sum of all the local blackbodies emitted by different annuli of the disc. By knowing the temperature of the innermost stable annulus of the disc, temperature of all the subsequent rings can be estimated. A simplified form of the temperature of the annulus at radius R is given by Equation 3.19 of Peterson (1997) (also see the ‘large r ’ approximation of Equation 5.43 of Frank, King & Raine (2002)). The same equation can be rewritten as:

$$T(R) = 3.5 \times 10^5 (\eta)^{-\frac{1}{4}} \left(\frac{\dot{m}}{\dot{m}_{\text{Edd}}} \right)^{\frac{1}{4}} \left(\frac{M_{\text{BH}}}{10^8 M_{\odot}} \right)^{-\frac{1}{4}} \left(\frac{R}{R_s} \right)^{-\frac{3}{4}} \text{ K} \quad (1)$$

M_{BH} is the mass of the central black hole, \dot{m} is its mass accretion rate, while \dot{m}_{Edd} is the Eddington mass accretion rate. $R_s = 2GM_{\text{BH}}/c^2$ is the Schwarzschild radius, G being the gravitational constant and c the velocity of light. η is the accretion efficiency factor, which relates

$$L = \eta \dot{m} c^2 \quad (2)$$

L being the luminosity emitted from the disk (both surfaces, top and bottom).

A standard model for the spectral component of a non-spinning accretion disc is available as a package called *diskbb* in XSPEC² (Mitsuda et al. 1984; Makishima et al. 1986). The two inputs required by *diskbb* are $T(R_{\text{in}})$ (which can be derived from 1) and the normalisation A_{dbb} , given by,

$$A_{\text{dbb}} = \left\{ \frac{R_{\text{in}}/\text{km}}{D/(10 \text{ kpc})} \right\}^2 \cos \theta \quad (3)$$

for a black hole observed at a distance D ($= 100$ Mpc throughout this paper) whose line-of-sight makes an angle θ ($= 30^\circ$ throughout this paper, unless otherwise mentioned) to the normal to the plane of the disc. R_{in} is the distance of the innermost stable annulus of the accretion disc from the central black hole.

To decide the value of $T(R_{\text{in}})$ for a black hole of mass M_{BH} , we have to consider the value of η carefully. Zimmerman et al. (2005) discuss that the *diskbb* assumes a nonzero torque at the inner boundary of the accretion disk (also see Gierlinski et al. 1999), which they refer to as the ‘standard torque’ scenario. In this scenario, the total luminosity of the disk is

$$L = \frac{3G\dot{m}M_{\text{BH}}}{2R_{\text{in}}} \quad (4)$$

(Equation 10 of Zimmerman et al. (2005)) Thus, using Equations 2 and 4, we see that η is dependant on the choice of R_{in} that we make

$$\eta = \frac{3GM_{\text{BH}}}{2c^2 R_{\text{in}}} \quad (5)$$

² <https://heasarc.gsfc.nasa.gov/docs/xanadu/xspec/>

For this paper, we adopt, $R_{\text{in}} = 3R_s = 6GM_{\text{BH}}/c^2$, for the non-spinning BH. Hence, $\eta = 0.25$.

With the above-mentioned definitions and assumptions, we have used the *diskbb* in version 11.3 of XSPEC to generate the SED (in flux - $f_{\nu}|_{\text{dbb}}$) of the radiation from one surface of the accretion disk. We can then obtain the luminosity from one surface of the disk, by multiplying with a factor of πD^2 and integrating over ν . We have verified using $\theta = 0$, in Equation 3, that the ratio of 2 times this luminosity, to the Eddington luminosity is $\simeq \dot{m}/\dot{m}_{\text{Edd}}$ used in Equation 1. The factor 2 is to account for emission from both sides of the disk.

After understanding this method of generating models for accretion disk radiation, we proceed to produce SEDs for the accretion disk, for a wide range of black hole masses - $M_{\text{BH}} = 10^6 - 10^{12} M_{\odot}$ - at steps of 0.25 dex. For demonstration, in the left panel of Figure 1, we plot the SEDs for the different masses (as labeled), but all of them for $L_{\text{dbb}}/L_{\text{edd}} = 0.1$ (solid-black lines), where L_{dbb} is the luminosity obtained by integrating the accretion disc SED (from *diskbb* in Xspec) through the entire energy range of $1 \mu\text{m} - 200\text{keV}$, and then converting from flux to luminosity through a factor of πD^2 . The drop in ionizing photons between the H ionization edge (912 Å) and the He ionization edge (228 Å) is large toward high masses. Note that the peak of the SEDs shifts towards the lower energies (or larger wavelengths) for heavier black holes. Even the SDSS filters (marked at the bottom of Figure 1, left panel) will probe a different part of the accretion disc for $M_{\text{BH}} \geq 10^9 M_{\odot}$, than that for standard mass black holes. Even for BHs with $M_{\text{BH}} = 10^8 M_{\odot}$ at redshift $z \geq 3$, these SDSS filters slide away from the $f_{\nu} \sim \nu^{1/3}$ region (which for each SED is highlighted by the thicker gray lines).

For most of the paper, we avoid the additional complication of the spin of the black hole. However, a spinning BH will have a harder SED shape in the photoionizing energy bands than a non-spinning BH of the same mass. Hence, after deriving the results for non-spinning SMBH, we perform an initial comparison of Schwarzschild and spinning BHs in Section 8.

2.2 The non-thermal radiation

In the energy range of 2keV-10keV, AGNs have a non-thermal spectral component that is ascribed to inverse Comptonization of some of the disc photons by the hot coronal plasma surrounding the black hole (Czerny & Elvis 1987; Lightman & Zdziarski 1987; Coppi 1992; Haardt & Maraschi 1993; Coppi 1999; Beloborodov 1999). This spectral component can be modeled using a power-law $f(\nu) \sim \nu^{-\alpha}$ where α is the spectral index (Arnaud 1996; Zdziarski, Johnson & Magdziarz 1996; Życki, Done & Smith 1999).

The power-law becomes a significant component in photoionizing the BEL ions, especially for HMBH SEDs, because the HMBH *diskbb* moves to lower energies.

Empirically α depends on L_{bol} (Lu & Yu 1999; Wang, Watarai & Mineshige 2004; Shemmer et al. 2006), though there is not complete consensus (Trakhtenbrot et al. 2017). Brightman et al. (2013) gives a phenomenological relation between the spectral index and L_{bol} as,

$$\Gamma = \alpha + 1 = (0.32 \pm 0.05) \times \log\left(\frac{L_{\text{bol}}}{L_{\text{Edd}}}\right) + (2.27 \pm 0.06) \quad (6)$$

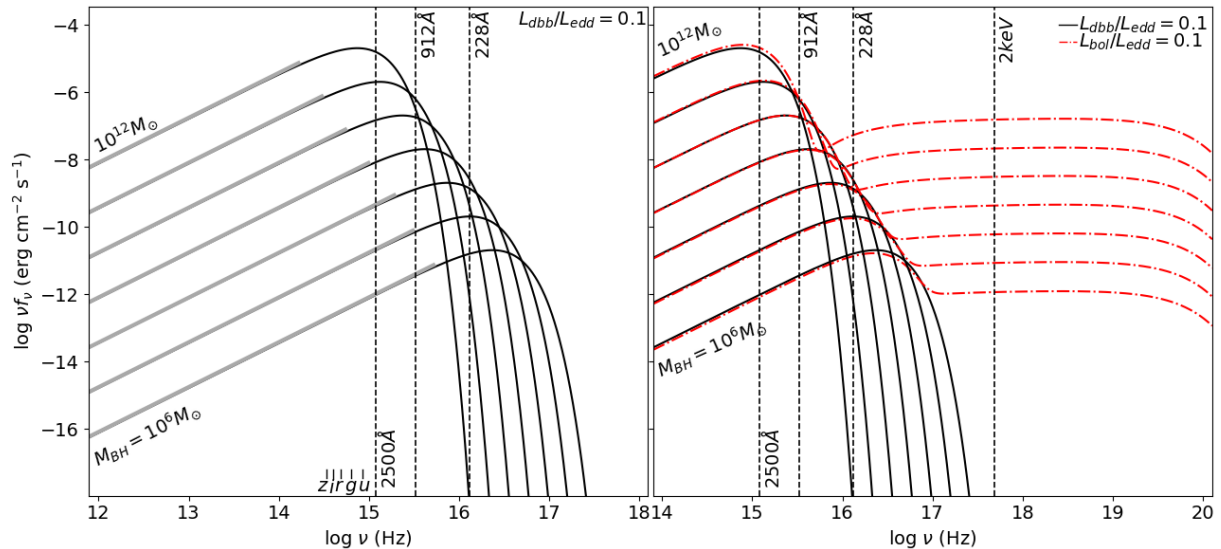


Figure 1. *Left Panel:* The spectral energy distributions (SEDs) of the radiation from the accretion disc around the super-to-hyper-massive black holes. The SEDs are calculated using the package *diskbb* within XSPEC. All the black holes here, are accreting at the rate $L_{dbb}/L_{edd} = 0.1$ and the different lines correspond to different black hole masses from $M_{BH} = 10^6 - 10^{12} M_\odot$ at steps of 1 dex. The gray thicker lines highlight the region of the SED where $f_\nu \sim \nu^{1/3}$. Note that the traditionally (since Tananbaum et al. (1979)) important wavelength 2500 Å does not fall in the gray part of the SED, unless $M_{BH} \lesssim 10^8 M_\odot$. We have also marked the positions of the centres of the five filters of SDSS, namely u, g, r, i and z. *Right panel:* The complete AGN SED from optical to X-rays (red dotted-and-dashed lines), but consisting of only the components from the central regions - the *diskbb* component, and the power-law component. The procedure of appropriately adding these two components to get the complete SED is elaborately described in Section 2. Note that the solid-black curves still correspond to $L_{dbb}/L_{edd} = 0.1$, whereas the dotted-and-dashed red curves correspond to $L_{bol}/L_{edd} = 0.1$. For details of this distinction, refer to Sections 2.1 and 2.3.

where L_{bol} is the total ‘observed’ Luminosity between 1μ and hard X-rays (200 keV). Note that the entire 1μ to 200 keV range cannot be observed - sometimes because of the natural extinction (by Galactic dust and neutral hydrogen) in the $\sim 10 - 200$ eV; and sometimes because of bad data in other wavelengths, for the samples that Brightman et al. (2013) considered. Hence they had made judicious extrapolations and modeling, where required. We then define L_{bol} as the sum of the luminosities from both the SED components - the accretion disc and the power-law, in the same energy range. Using Equation 6, we see that the spectral indices for power-law components will be 0.78, 0.95, 1.10 & 1.27 respectively, for the different $L_{bol}/L_{edd} = 0.03, 0.1, 0.3$ and 1.0 ratios that we plan to investigate in this paper. Note that, in this paper, we shall use L_{bol}/L_{edd} as proxy for the accretion rate. Using these spectral energy indices we construct power-law component and introduce exponential cut-offs at both the ends.

$$f(\nu) \sim \nu^{-\alpha} \times e^{-\frac{10eV}{\nu}} \times e^{-\frac{\nu}{200keV}} \quad (7)$$

Once the power-law component is constructed, we need to devise a scheme for its relative normalisation with respect to the *diskbb* component.

2.3 The multicomponent broad-band AGN SED

Conventionally, the nominal UV to X-ray slope, $\alpha_{OX} = -0.384 \log(L_{2keV}/L_{2500\text{\AA}})$ (Tananbaum et al. 1979) is used to relate the luminosities at 2500 Å and 2 keV, where the accretion disc radiation predominantly determines the luminosity at 2500 Å, while the X-rays at 2 keV mostly comes

Table 1. Maximum M_{BH} for which 2500 Å falls on the linear part of their SED.

$\frac{L_{bol}}{L_{edd}}$	$\log(\frac{M_{BH}}{M_\odot})$
0.03	7.75
0.1	8.25
0.3	9.00
1.0	9.25

from the power-law component. For the BHs in the ‘standard AGN mass range’, $M_{BH} \lesssim 10^8 M_\odot$, and $L_{bol}/L_{edd} \gtrsim 0.1$, 2500 Å falls on the part of the *diskbb* SED, where $f_\nu \sim \nu^{1/3}$ (thick highlighted gray lines in the left panel of Figure 1). However, for HMBHs the peak of the *diskbb* emission moves to lower energies and $f_\nu \sim \nu^{1/3}$ may not be satisfied at 2500 Å, as demonstrated in left panel of Figure 1. The highest possible black hole mass, for which 2500 Å deviates from $f_\nu \sim \nu^{1/3}$, is also a function of the accretion rate, L_{bol}/L_{edd} . For the different L_{bol}/L_{edd} ratios, used in this paper, in Table 1, we have listed the values of the highest mass for which 2500 Å, in the corresponding SEDs, falls on the $f_\nu \sim \nu^{1/3}$ part of the *diskbb* SED. Thus, for HMBHs, 2500 Å represents a physically different part of the accretion disc than in case of the standard mass black holes. The reason we pay due attention to the nature of the SED at 2500 Å, is because this wavelength has been used as a reference wavelength in many multiwavelength AGN SEDs, even for the more recent, robust, SED investigations, where Ultraviolet and optical luminosities are related to each other. Lusso & Risaliti

Table 2. Constants of the $\log(\frac{M_{BH}}{M_\odot}) - \frac{L_{pl}}{L_{dbb}}$ best-fit equation.

$\frac{L_{bol}}{L_{Edd}}$	a_1	a_2	b_2
0.03	-8.21633	165.093	-3.58592
0.1	-1.35708	21.282	-0.523004
0.3	-1.30806	23.599	-2.24452
1.0	-0.674781	12.5449	-2.31223

(2016) examined a large sample of 159 AGN and found a tight relationship between the luminosities at 2500Å and 2 keV.

$$\log(L_{2keV}) = 0.638 \times \log(L_{2500}) + 7.074 \quad (8)$$

While they use the same wavelengths, as used by the definition of α_{OX} , this form of the relationship directly relates the observables, namely the fluxes.

For each L_{bol}/L_{edd} , we first choose the range of M_{BH} for which the 2500Å falls on the part of the *diskbb* SED, where $f_\nu \sim \nu^{1/3}$. For example, as seen from Figure 1 (left panel) and Table 1, for $L_{dbb}/L_{edd} = 0.1$ this mass range corresponds to $M_{BH} = 10^6 M_\odot$ to $10^{8.25} M_\odot$. For each of these SEDs, we then scale the power-law component relative to the *diskbb* as follows. For each value of M_{BH} , we start with $L_{dbb}/L_{edd} = \text{desired } L_{bol}/L_{edd} = 0.1$ (say). The XSPEC generated *diskbb* spectra give us the value of L_{2500} . Thus, we can use that value in Equation 8 to derive L_{2keV} , which gives us the required normalisation for the power-law component. We add the luminosity L_{dbb} in the *diskbb* and the luminosity L_{pl} in the normalised power-law component and check if $L_{bol}/L_{edd} = 0.1$. If $L_{bol}/L_{edd} \neq 0.1$, then we iterate by changing L_{dbb}/L_{edd} slightly, and repeating the process. The iteration continues, until, for the given M_{BH} , we achieve $L_{bol}/L_{edd} = (L_{dbb} + L_{pl})/L_{edd} = 0.1$. At this stage, we calculate the luminosity (L_{pl}) in the power-law component and the luminosity in the (L_{dbb}) in the *diskbb* component, whence we can derive the ratio L_{pl}/L_{dbb} . In Figure 2, the red circles correspond to the mass range for which the ratio L_{pl}/L_{dbb} was derived using the aforementioned method. The solid black line joining the red circles is then extrapolated using a smooth, power series extrapolation,

$$\frac{L_{pl}}{L_{dbb}} = \frac{a_1}{\frac{M_{BH}}{M_\odot}} + \frac{a_2}{(\frac{M_{BH}}{M_\odot} - b_2)^2} \quad (9)$$

where the values of constants are provided in the Table 2. Thus, for the higher mass black holes, as well, we get the scaling of the power-law component relative to the *diskbb* component, which can then be used to construct the corresponding SEDs. We have thus, built a suite of SEDs (100 of them) for $L_{bol}/L_{edd} = 0.03, 0.1, 0.3, 1.0$ with the range of mass varying from $M_{BH} = 10^6 M_\odot$ to $10^{12} M_\odot$ in intervals of 0.25 dex. The right panel of the Figure 1 shows the optical to X-rays SEDs (red dotted-and-dashed lines) obtained thus, for $L_{bol}/L_{edd} = 0.1$, where the steeply falling (relative to the power-law) higher energy tails of the *diskbb* are shown in solid black lines. Above $M_{BH} \sim 10^9 M_\odot$ the power-law dominates the main ionizing continuum relevant for the BEL ions. For lower accretion rate ($L_{bol}/L_{edd} < 0.1$) this statement is true for even lower black hole mass.

One might argue that Equation 8 does not distinguish

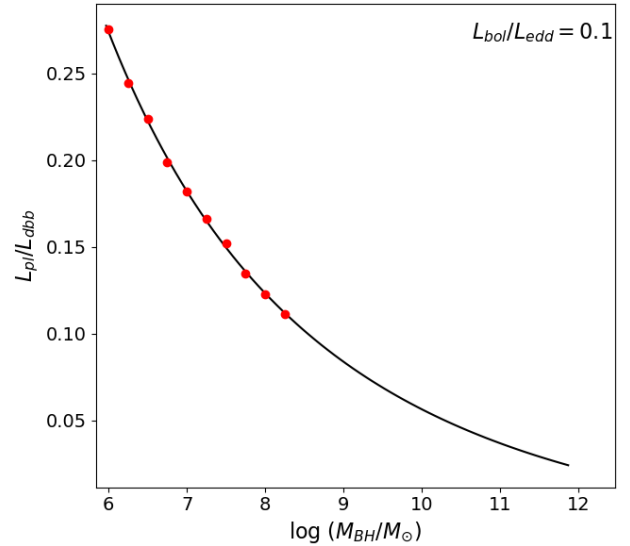


Figure 2. L_{pl}/L_{dbb} ratios as a function of mass ratios for $L_{bol}/L_{edd} = 0.1$. Red circles are the ratios obtained by using Eq. 8 to derive L_{2keV} . The red circle with the highest mass represents the highest mass black hole for which 2500 Å falls within the $f_\nu \sim \nu^{1/3}$ part of the SED. Black line represents the best-fitting curve through the red circles and is further extrapolated to find the L_{pl}/L_{dbb} ratios for higher masses, using the fit function Eq. 9.

between super and hyper massive black holes and so this equation should be used directly, even for the HMBHs and we should not extrapolate. However, these extrapolations, which become important only for the HMBHs, are based on the physics of accretion discs. Further, in Section A, we show that if we had directly used Equation 8 for the highest masses, the differences in the results would be minor, and effectively has no difference in the qualitative inferences.

3 PHOTOIONIZATION CALCULATION

For each of 100 SEDs (25 masses \times 4 L_{bol}/L_{edd} values), we use the C17.00 version of CLOUDY³ (Ferland et al. 2017), to calculate the EWs of many emission lines for a wide range of the parameters $\Phi(H)$, n_H and N_H . $\Phi(H)$ is the ionizing incident photon flux $\Phi(H) = Q(H)/4\pi r^2$, where $Q(H)$ is the number of Hydrogen ionizing photons.

Though CLOUDY gives EW of each line as a function of $\Phi(H)$, n_H , the parameter $\Phi(H)$ can easily be interchanged by r . Hence, we can express (following Hazy 2) that the flux of the emission line from a cloud of density n_H and at a distance r is

$$F(r, n_H) \sim EW(r, n_H) \frac{\nu F_\nu^c}{\lambda} \quad (10)$$

where λ is the central wavelength of the line and νF_ν^c is the incident continuum at λ . $F(r, n_H)$ can then be used in Eq. 12 to calculate the total line luminosity L_{line} , as described in the next section.

For the calculation of BELs, the parameters are stepped over a grid of values as shown in Table 3, a total of 845

³ <http://www.nublado.org/>

Table 3. BEL parameter ranges

	min	max	Δ
$\log \Phi(H)$	18	24	0.5
$\log n_H$	8	14	0.5
$\log N_H$	21	23	0.5

Table 4. NEL parameter ranges

	min	max	Δ
$\log \Phi(H)$	10	20	0.5
$\log n_H$	2	10	0.5
$\log N_H$	21	23	0.5

CLOUDY runs (for each SED). These ranges are based on Baldwin et al. (1995), Korista et al. (1997a) and the range of N_H on Chakravorty et al. (2014). We have calculated the EWs of all the 42 prominent quasar emission lines listed in (Korista et al. 1997a), out of which only 5 strongest lines are demonstrated here.

For the calculation of NELs, the ranges in Table 4 were used. We adopted these ranges based on Ferguson et al. (1997). We have calculated the EWs of all the 23 prominent narrow emission lines listed in Ferguson et al. (1997), out of which only 6 strongest lines are demonstrated here. For NELR, the presence of dust can play some role in determining the gas composition and hence the strength of lines. Ferguson et al. (1997) demonstrate the effect of the presence of dust in detail. However, they also find a combination of parameters, where the dust-free gas produces very similar line strengths (matching observations) as a dusty gas. For the sake of simplicity, we adopt those parameters and work with dust-free gas for the NELR. The appropriate parameters are discussed in more details in Section 6.

Thus for the total number of SEDs explored in this paper, along with the calculations for each of the physical parameters of the gas properties $\Phi(H)$, n_H and N_H , we ran a total of 256,240 CLOUDY models. For SEDs with low accretion rate, we have done CLOUDY calculations only up to $M_{BH} = 10^{11.5} M_\odot$ due to numerical convenience. This huge theoretical data set was then used to calculate the optimal line strengths as discussed in the next Section (4).

4 LOCALLY OPTIMALLY EMITTING CLOUDS

Strong BELs are the identifying feature of AGN and study of them gives information on their central engine. The BELs are also used to estimate the chemical composition of the hosting galaxy and their EWs are even used in estimating the black hole mass.

Photoionization models of the broad line region are extremely relevant to the study of AGN (Netzer, Laor & Gondhalekar 1992). Early BLR models were quite limited and used to assume the lines were emitted by the single gas cloud, one with a single ionization parameter, column density and gas density (Kwan & Krolik 1981). These models became untenable when reverberation mapping observa-

tions showed the presence of a wide distribution of emission-line cloud properties with distance from the ionizing continuum. This development prompted a multi-cloud model with a wide range of spatial and density distributions (Baldwin et al. 1995).

The “locally-optimally emitting cloud” (LOC) model was introduced by Baldwin et al. (1995). This model established that any given BEL is most intensely emitted by gas with a particularly narrow range of ionization parameter and density and thus a weighted average over spatial and density distribution includes the gas with optimal parameters for each of the observed lines. Ferguson et al. (1997) further extended this model to predict the line strengths of Narrow Emission Lines (NELs).

The total line luminosity emitted by the entire set of clouds at various radial distances and densities is given by,

$$L_{line} \propto \int \int r^2 F(r, n_H) f(r) g(n_H) dn_H dr \quad (11)$$

where $f(r)$ and $g(n_H)$ are the spatial and density distribution functions respectively. For simplicity we assume them to be power laws as in Ferguson et al. (1997). We have further normalised the L_{line} over the entire spatial and density distribution functions.

$$L_{line} = 0.24 \frac{\int \int r^2 F(r, n_H) r^\gamma n_H^\beta dn_H dr}{\int \int r^\gamma n_H^\beta dn_H dr} \quad (12)$$

Similarly, the weighted average of the EWs (\mathcal{EW}) of each line emitted by the entire set of clouds at various radial distances and densities is calculated using,

$$\mathcal{EW} = 0.24 \frac{\int \int EW(r, n_H) r^\gamma n_H^\beta dn_H dr}{\int \int r^\gamma n_H^\beta dn_H dr} \quad (13)$$

The successes and the limitations of LOC model are discussed in detail by Leighly & Casebeer (2007). Limitations of LOC model include that (i) some parameters, like the spatial and density indices cannot be physically interpreted and (ii) a number of physical effects are not included in the model, a significant one being self-shielding. However, for the purpose of this paper, the LOC model is sufficient.

The factor 0.24 in Equations 12 and 13 represents a nominal constant covering factor for the broad line emitting clouds (following Leighly & Casebeer 2007, see Figure 1). Covering fraction is a very complex issue, varying from source to source. Hence its theoretical generalisation over a wide range of mass and accretion rates of BHs is difficult and beyond the scope of this paper. Hence we maintain this value of 0.24 throughout the paper, even for narrow line emitting clouds. Please note that any different constant covering factor would simply scale the $\log(\mathcal{EW})$ s in the vertical direction, in our subsequent Figures, altering none of the trends demonstrated. Further, a constant covering factor will absolutely have no effect of the line ratios, presented later.

5 BROAD EMISSION LINES

From the CLOUDY photoionization calculations, we derive EWs for all the prominent BELs. The EWs are measured relative to the incident continuum at 1215 Å which is then normalised to the central wavelength of each line. In Figure

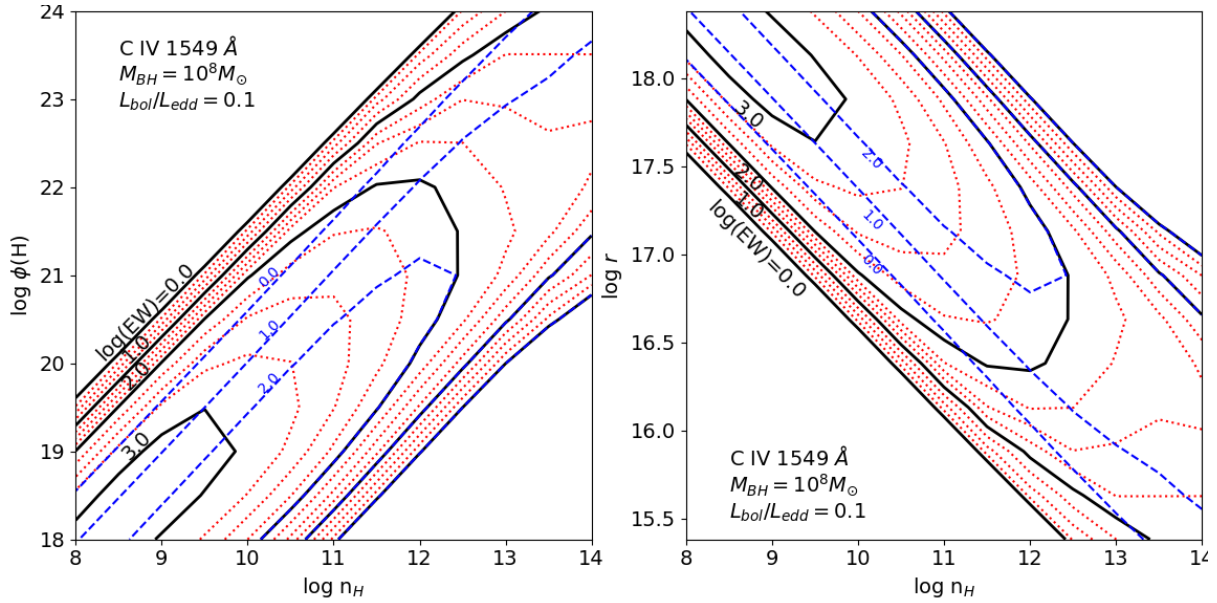


Figure 3. Contour plot for EW of C IV (1549 Å) in the $n_H - \Phi(H)$ plane (left panel) and $n_H - R_{cloud}$ plane (right panel). The solid black lines are contours at steps of 1 dex and dotted red lines are at the steps of 0.25 dex, for $\log N_H = 23$. The dashed blue lines are contours at steps of 1 dex, for $\log N_H = 21$. Originally, Baldwin et al. (1995) and Korista et al. (1997) presented the efficiency of line emission for different BELs as a function of n_H and Φ (as in the left panel). Ferguson et al. (1997) made a similar study on NELs; efficiency was presented as a function of n_H and R_{cloud} (as in the right panel) instead. For the sake of consistency, between the BEL and NEL analysis we stick to R_{cloud} instead of Φ , throughout the rest of this paper. Here, we represent both planes, to demonstrate that it is a mere inversion of the contours, when the y-parameter of the plane is changed from Φ to R .

3 we represent the iso-contours of calculated EWs (in log) for C IV 1549 Å, one of the strongest known broad emission lines on the $\log n_H - \log \Phi(H)$ (left panel) and $\log n_H - \log r$ (right panel) planes for $M_{BH} = 10^{8.0} M_\odot$ and $L_{bol}/L_{Edd} = 0.1$. We see that our (solid-black and dotted-red) contour plots match closely with the contours presented in Baldwin et al. (1995) and Korista et al. (1997a), for $\log N_H = 23$. The slight quantitative differences are expected because the earlier authors used a slightly different SED compared to the one that is used to get Figure 3. The diagonal lines in the contours with a slope of 45° are of constant ionization parameter $U = \Phi(H)/cn_H$, which is a measure of the recombination rate at the face of the cloud. C IV being a collisionally excited line shows a band of constant U lines where there is efficient emission. At high n_H and $\Phi(H)$, contours start to turn over indicating thermal heating of the gas instead of photoionization. To understand the effects of column density we point to the isocontours for $\log N_H = 21$ in dashed blue line, in Figure 3. When compared to the solid-black $\log N_H = 23$ contours (at same 1 dex separation), the ones with lower N_H show that for highly ionized gas, we need high column density gas to yield emission lines of any reasonable strength. In Figure 4, we represent the contour for $M_{BH} = 10^{11} M_\odot$ to compare the efficiency of line emission at higher masses. While the highest EW achieved for the $M_{BH} = 10^8 M_\odot$ SED is $10^{2.5}$, that for the $M_{BH} = 10^{11} M_\odot$ SED is $10^{1.25}$. Thus, everything else remaining the same, the line becomes fainter by 1.25 dex.

To assess the contribution from all the clouds spread across a range of distance and having a range of density, we apply the LOC model mentioned in Section 4 for our calculations. We use Eq. 12 and Eq. 13 over the entire range of

r and n_H . Baldwin (1997) suggested that the L_{line} is only weakly sensitive to the radial and column density distributions as long as γ in Eq. 12 is > -1 . Baldwin (1997) further shows that $\beta = -1$ is strongly suggested by observations which is further confirmed by Hamann et al. (2002). Therefore, we use a constant power index of -1 for both, n_H and r in our calculations to get L_{line} and \mathcal{EW} . Figure 5 shows the resultant $\log(\mathcal{EW})$ as a function of M_{BH} for the BEL C IV 1549 Å, for $L_{bol}/L_{Edd} = 0.1$ (red dotted line).

At $10^4 K$, thermal widths are only about 10 km s^{-1} . The observed widths in BELs ($\gtrsim 10 \text{ km s}^{-1}$) should, therefore, be due to organised high velocity flows of clouds with Keplerian, or at least, virialised velocities. This allows us to define maximum radius for BLR as,

$$R_{Keplerian} = GM_{BH}/v_{min}^2 \quad (14)$$

where v_{min} is the lowest observed velocity of the cloud. Introducing $R_{Keplerian}$ cut-off within CLOUDY calculated line strengths, results in a significant change in \mathcal{EW} at the lower mass end as in Chakravorty et al. (2014). In Figure 5, the black solid line corresponds to \mathcal{EW} after imposing a lower limit at $v_{min} \geq 1000 \text{ km s}^{-1}$. For the rest of the paper, we will always calculate \mathcal{EW} and L_{line} for (all) BELs, maintaining this lower limit of v_{min} .

In the different panels of Figure 6, we extend the calculation and show how the line strength \mathcal{EW} of six of the prominent BELs such as O VI 1034 Å, C IV 1549 Å, He II 1640 Å, Mg II 2798 Å, H β 4861 Å and H α 6563 Å vary when accretion rate is varied over the range $0.03 \leq L_{bol}/L_{Edd} \leq 1.0$.

For C IV 1549 Å (top middle panel of Figure 6) at $L_{bol}/L_{Edd} = 0.1$ the $\mathcal{EW} = 26$ for the $10^8 M_\odot$ BH, which is in excellent agreement with what Figure 1 of Leighly &

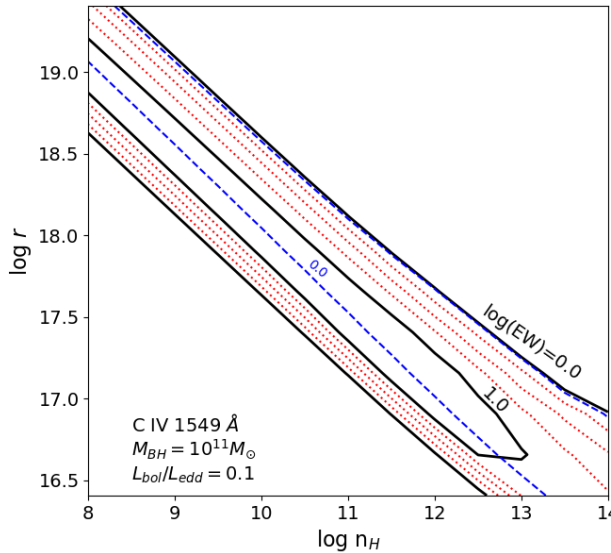


Figure 4. Contour plot for EW of C IV (1549 Å) in the $n_H - R_{cloud}$ plane for $M_{BH} = 10^{11} M_{\odot}$. The efficiency of the line emission has decreased greatly when compared to $M_{BH} = 10^8 M_{\odot}$ (Figure 3). The different line styles and colours represent the same variation of physical parameters as in Figure 3.

Casebeer (2007) predicts for the same emission line, for the nominal model (with $C_f = 0.24$). The \mathcal{EW} of this line remains quite constant for $10^6 M_{\odot} < BH < 10^8 M_{\odot}$ and then drops quickly to 1% of the peak by $\sim 10^{10} M_{\odot}$. O VI 1034 Å, He II 1640 Å and Mg II 2798 Å all show similar ~ 2 dex decrease in \mathcal{EW} from $10^8 M_{\odot}$ to $10^{10} M_{\odot}$. H β 4861 Å and H α 6563 Å show similar behavior from $10^9 M_{\odot}$ to $10^{11} M_{\odot}$.

In Figure 6 notice the distinction between the \mathcal{EW} profiles of the high ionization O VI, C IV, and He II (top panels) to those of the low ionization Mg II, H β and H α lines (bottom panels). The low ionization lines maintain quite constant \mathcal{EW} up to $\sim 10^{10} M_{\odot}$ while the high ionisation lines begin to drop in \mathcal{EW} by $\sim 10^8 M_{\odot}$, for the BHs with accretion rate $L_{bol}/L_{edd} = 0.1$. The aforementioned mass ranges mentioned for the \mathcal{EW} profiles vary when the accretion rate changes, but the qualitative behaviour of the different lines remains the same. Also, the high ionization profiles decrease with increase of mass, up to a critical value of BH mass, hit a minimum and then invert the trend and start increasing with mass. On the other hand, the low ionization lines show increase (or almost constant values) of \mathcal{EW} with mass increase, hit a maximum and then drops with increase in mass. Such differing evolution of the \mathcal{EW} s will also have consequences on how the luminosities of these lines would evolve as a function of the BH mass, particularly at the high mass end.

We take C IV 1549 Å as a representative of the high ionization lines and H α 6563 Å as a representative of the low ionization lines and plot their luminosities as a function of mass in Figure 7. At the high mass end, while the luminosity of the C IV line remains constant, the luminosity of H α line drops, sometimes by even an order of magnitude. *Thus the low ionization lines are not the best tracers to look for while searching for the HMBH using the current optical telescopes. This result has implications for the most commonly done BH searches that rely on optical surveys like*

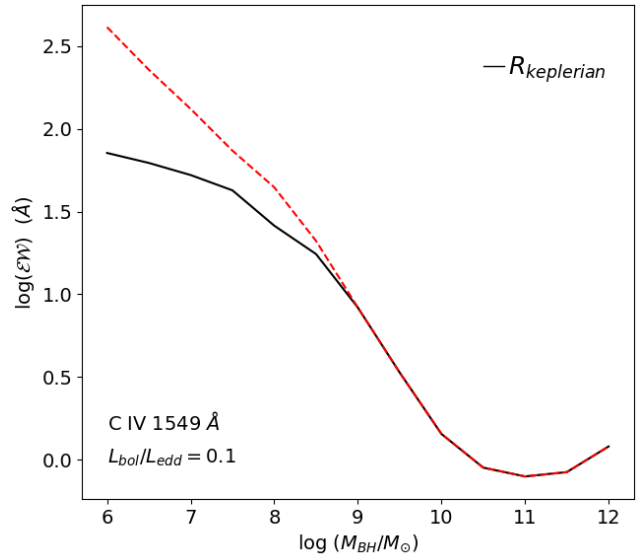


Figure 5. \mathcal{EW} of C IV (1549 Å) as a function of M_{BH}/M_{\odot} . Dashed line represents \mathcal{EW} calculated using LOC integration (Equation 13). The black solid line represents \mathcal{EW} after limiting the outermost radius of cloud with $v_{min} = 1000 \text{ km s}^{-1}$.

SDSS, which in their turn, rely heavily on the H β 4861 Å and H α 6563 Å lines. However, the results presented here may serve as a benchmark for emission line studies, using the next generation 30 m class optical telescopes.

The distinction between the behaviour of the high and the low ionization lines is readily understood from Figure 8. The ionization potentials (IP) of O VI and C III, which would result in the formation of O VI and C IV ions, are the highest, among the BEL ions/elements discussed. Note that the IP of these ions are at an interesting energy range - one where the accretion disc is more dominant for the SEDs of the lower mass ($M_{BH} \lesssim 10^8 M_{\odot}$) black holes, but the power-law radiation component is more dominant for the higher mass BHs. For each ion (high ionization lines), the narrow mass range, where the transition of the relative dominance happens, is where the \mathcal{EW} turns over. For ions (low ionization lines), where there is no significant switch of the dominating SED component, the \mathcal{EW} simply declines with an increase in BH mass. In fact, for the H α and H β lines from **neutral**, but excited Hydrogen, of course IP is not the deciding factor. Hence, they follow the simple rationale that the \mathcal{EW} increases with the mass (and hence the luminosity) of the BH until their line energies go above the $f(\nu) \sim \nu^{1/3}$ part of the BH SED - which happens because the accretion disc peak and hence the $\nu^{1/3}$ (part of the SED) recedes to lower energies with an increase in BH mass. Thus, at the corresponding BH mass, the H α and H β \mathcal{EW} s start dropping. This discussion thus illustrates the fine sensitivity that line strengths have on the shape of the illuminating SED. Further, this sensitivity becomes evident in our study because we are probing a mass range of BHs where the SEDs transition through the energy range of the relevant IPs and line energies - a very fortunate natural coincidence indeed!

Figure 6 further shows that the turn around of $\log(\mathcal{EW})$ in O VI 1034 Å, C IV 1549 Å for higher masses makes it impossible to determine the mass of the HMBH accurately

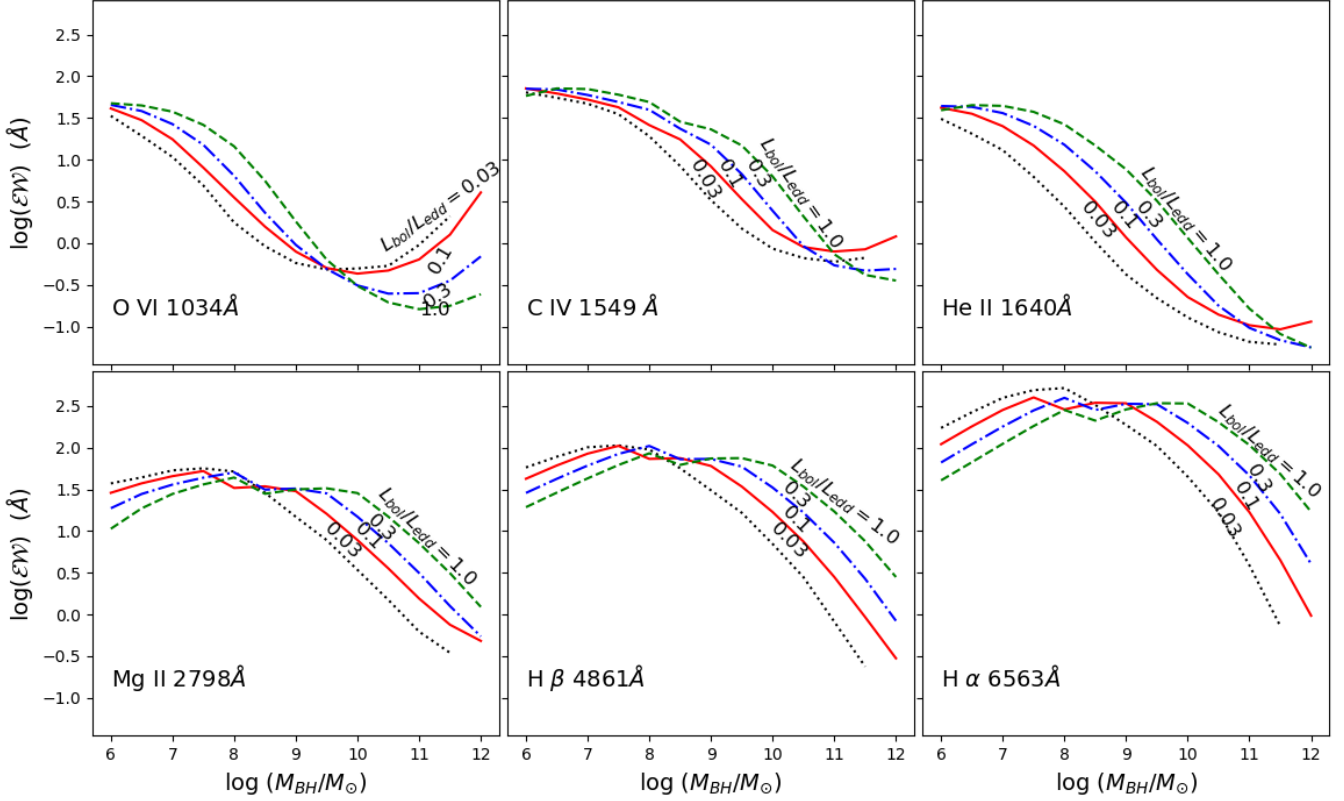


Figure 6. Evolution of \mathcal{EW} of few prominent BELs over range of masses and accretion rates.

using just $\log(\mathcal{EW})$ of these strong BELs. For the other emission lines, similar degeneracy exists at the lower mass end. Hence, to remove this degeneracy we have calculated line ratios which we discuss in Section 7.2.

We are in a position to investigate if the Baldwin Effect (Baldwin 1977; Zheng & Malkan 1993; Shemmer & Lieber 2015) holds true for the HMBHs and gain some insight on the mass range or range of accretion rates for which this effect remains valid. Hence, we plot the \mathcal{EW} of C IV 1549 Å as a function of $L_\nu(1450)$ in Figure 9. The left-most thick solid magenta line in Figure 9 shows the relationship, $\mathcal{EW} \sim L_\nu^{-2/3}(1450)$, predicted by Baldwin (1977) between the C IV line strength and the Luminosity at 1450. Clearly, the low mass BHs ($M_{BH} < 10^7 M_\odot$) do not obey this relationship. However, for higher masses ($10^8 \leq M_\odot \leq 10^{11}$), the match with the slope of $-2/3$ ($= -0.66$) is good and improves for higher accretion rates; albeit the mass range where the match is better, also shifts to the higher values with the increase in accretion rate. For $L_{bol}/L_{Edd} = 0.03$, the slope is -0.51 for mass range $10^7 - 10^{10} M_\odot$, for 0.1 , the slope is -0.53 for $10^8 - 10^{11}$, for 0.3 , the slope is -0.66 for $10^9 - 10^{11}$ and finally, for 1.0 , the slope is -0.63 for $10^9 - 10^{12}$. Beyond $10^{11} M_\odot$, the Baldwin effect disappears as the \mathcal{EW} of the C IV line starts to strengthen again, especially, at low accretion rates. Thus, we show that the Baldwin effect is a natural result of the changing accretion disk SED with BH mass over 2 - 4 orders of magnitude.

Note that the discussion of the behaviour of emission line strengths in this section is for non-spinning black holes. To understand how BH spin may play a role (particularly

for the OVI and the CIV lines) in this discussion, refer to Section 8.

6 NARROW EMISSION LINES

We want to know if the NELs will have different observable properties as mass of the BH rises. Hence, we conducted CLOUDY simulations of the NELs, as well. In the left panel of Figure 10 we show the iso-contours of calculated EWs (in log) for the [O III] 5700 Å line in the $\log n_H$ - $\log r$ plane for $M_{BH} = 10^{8.0} M_\odot$ and $L_{bol}/L_{Edd} = 0.1$. As mentioned in Section 3 (Table 4), we are using a different range of Φ and n_H for NELs (as opposed to the right panel of Figure 3). As NLRs are situated further away from the BLRs, the range of $\Phi(H) = Q(H)/4\pi r^2$ for which NELs are efficiently produced is lesser than that of BELs (Peterson 1997). The EWs are measured relative to the incident continuum at 4860 Å which is then normalised to the central wavelength of each line. We see that our contour plots match closely with the contours presented in Ferguson et al. (1997) for $\log N_H = 23$. The small differences are because of the slightly different SED that we use. In the right panel of Figure 10, we represent the contour for $M_{BH} = 10^{11} M_\odot$ to compare the efficiency of line emission at higher masses. While the highest EW achieved for the $M_{BH} = 10^8 M_\odot$ SED is $10^{3.75}$, that for the $M_{BH} = 10^{11} M_\odot$ SED is $10^{1.25}$. Thus, everything else remaining the same, the line becomes fainter by 2.5 dexes.

Over the entire range of parameter space, we used CLOUDY to calculate the line strengths for almost all of the lines discussed in Ferguson et al. (1997). However, for

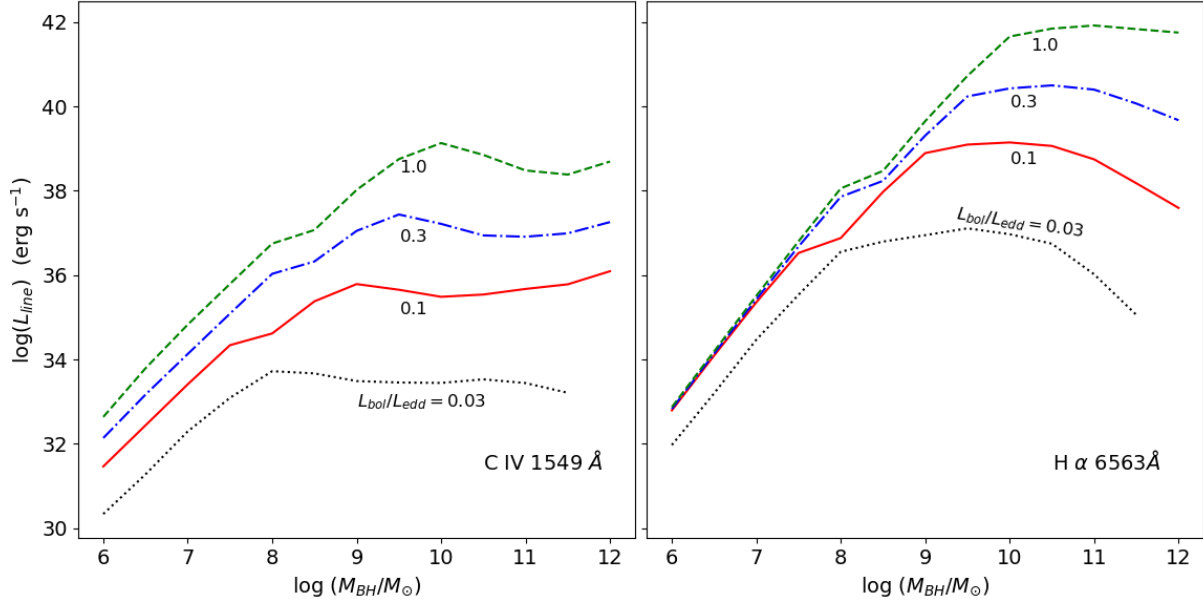


Figure 7. L_{line} of C IV 1549 Å and H α 6563 Å as a function of M_{BH}/M_{\odot} calculated using Eq. 13.

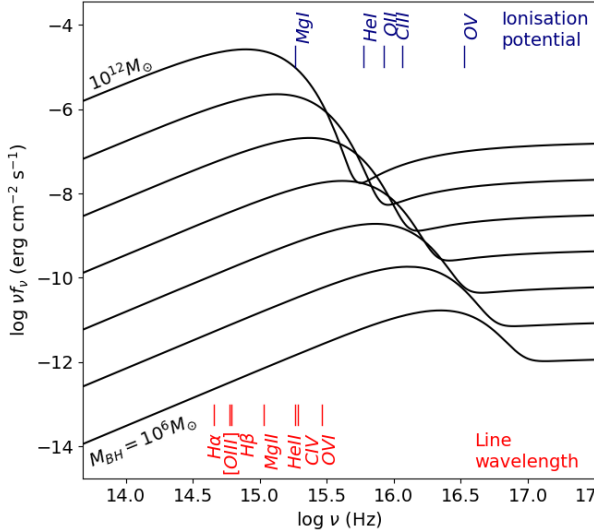


Figure 8. The line wavelength of the 5 strongest BELs (marked at the bottom) and the ionization potentials of the lower ions (marked on the top) are compared against the shape of the broad band SEDs of different BHs, for $L_{bol}/L_{edd} = 0.1$.

the scope of this paper, we use results of 6 of them, namely Hβ 4861 Å, [O III] 5007 Å, [O I] 6300 Å, Hα 6563 Å, [N II] 6584 Å and [S II] 6720 Å. The individual EWs were then used in Eqs. 12 and 13 to calculate L_{line} and \mathcal{EW} . The sensitivity of γ and β of Eq. 12 in case of NELs are presented in detail in Ferguson et al. (1997) and shows that for dust-free models like ours, $\gamma = -1.25$ and $\beta = -1.4$ fits the observational spectra the best. Hence, we use these indices for our calculations. In the case of BELs, we had used an upper limit for $r(=R_{keplerian})$ corresponding to $v_{min} = 1000$ km/s. To make a clear distinction between BLR and NLR, we use a similar idea, but this time for lower limit of $r(=R_{keplerian})$ corresponding to $v_{max} = 500$ km/s. The results are shown in Figure 11 (main panel). Note that unlike some of the BELs

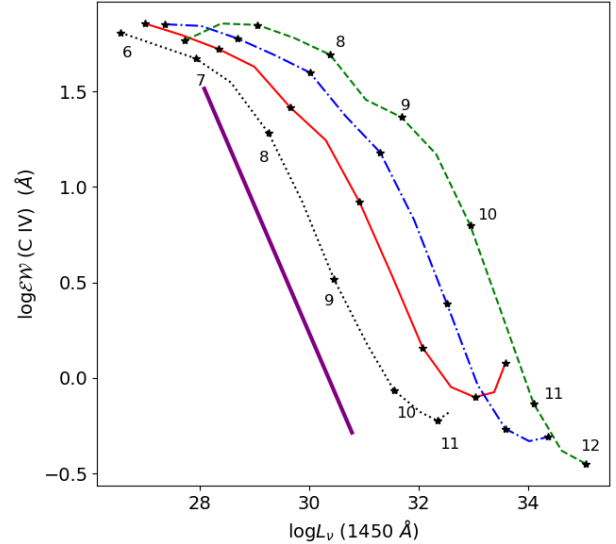


Figure 9. Demonstration of the Baldwin effect using the CIV 1549 Å emission line. The left-most thick solid magenta line is the predicted Baldwin effect relationship $\mathcal{EW} \sim L_{\nu}^{-2/3}(1450)$, with arbitrary normalisation. The rest of the lines are the (EW) profiles of the C IV line, having the same line-colour description as in Figure 6 - from accretion rate of 0.03 to 1.0, from left to right. The numbers on each profile indicate the mass of the BH, in $\log(M_{BH}/M_{\odot})$.

(O VI 1036 Å, CIV 1549 Å and He 1640 Å), the EW of [O III] 5007 Å line decreases monotonically with the increase in the mass of the black hole. \mathcal{EW} of [O III] 5007 Å drops by ~ 1.5 dex from $M_{BH} = 10^8 M_{\odot}$ to $10^{10} M_{\odot}$. This amplitude is similar to those seen for most of the BELs. The same behaviour holds for all 6 NELs that we are discussing in this paper.

To understand the evolution of the [O III] 5007 Å line \mathcal{EW} , we again refer to Figure 8. The ionization potential of O II is similar to that of He I, but the corresponding [O III] line

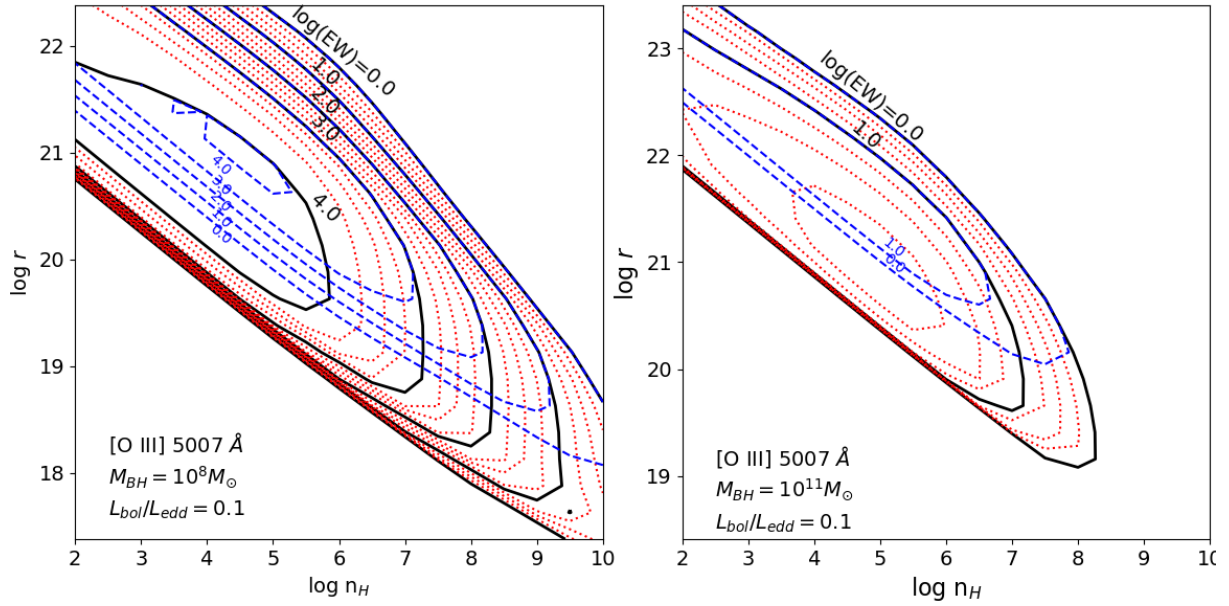


Figure 10. Contour plot for EW of [O III] 5007 Å in the $n_H - r$ plane for $M_{BH} = 10^8 M_\odot$ (left panel) and $10^{11} M_\odot$ (right panel). The solid black lines are contours at steps of 1 dex and dotted red lines are at the steps of 0.25 dex, for $\log n_H = 23$. The dashed blue lines are contours at steps of 1 dex, for $\log n_H = 21$. It is evident that the efficiency of the line emission has decreased greatly in $M_{BH} = 10^{11} M_\odot$ when compared to $M_{BH} = 10^8 M_\odot$.

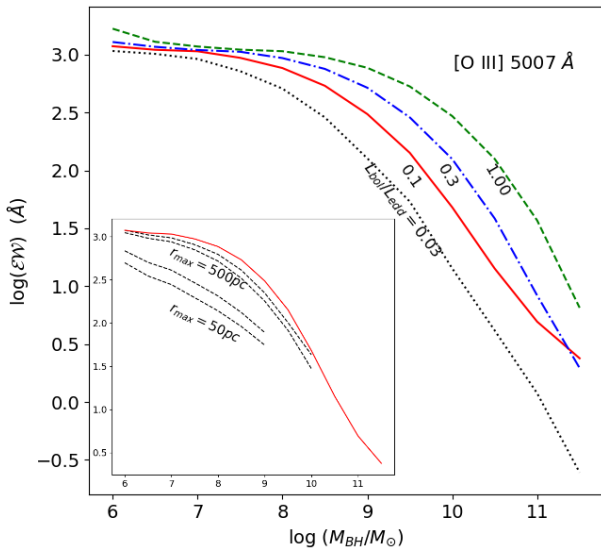


Figure 11. $\log \mathcal{EW}$ of [O III] 5007 Å as a function of $\log M_{BH}/M_\odot$ for different L_{bol}/L_{edd} . In the inset panel, we have compared, for accretion rate 0.1, modified \mathcal{EW} s where the LOC integration was done up to $r = 1000, 500, 100, 50$ pc (dashed black lines, from top to bottom, respectively)

does not exhibit a turnover in EW, similar to that of He II 1640 Å broad emission line. The EW profile is rather similar to that of the Hydrogen lines H α and H β , indicating that it is the shape of the SED at the energy range of the [O III] line's central wavelength, that determines the strength of the line. Because [O III] 5007 Å, is a forbidden line, it is the energy (of the illuminating SED) at the central wavelength of the line, that is of more importance than the energy at the IP of O II, as explained by the Stoy energy balance temperature

indicator (see section 5.10 of [Osterbrock & Ferland 2006](#)). The evolution of the \mathcal{EW} of all the other 5 NELs would be similar to that of [O III] 5007 Å, because they too are forbidden lines.

The \mathcal{EW} s of O III 5007 Å \mathcal{EW} s are higher from that usually observed for the O III line ($\lesssim 100$ - Figure 1 of [Risaliti, Salvati & Marconi \(2011\)](#) shows a distribution; also see [Shen et al. \(2011\)](#)). One reason for the discrepancy is because we did not put any constraint on the upper limit of r in the LOC integration of NELs. We demonstrate the effect of incorporating this constrain in the inset of Figure 11. notice the comparison, with the solid red curve, of the modified \mathcal{EW} s as the upper limit on r is varied from 1000 pc to 50 pc, through 500 and 100 pc. For the $r_{max} = 100$ pc profile, we see that for the $10^8 M_\odot$ BH, $\log(\mathcal{EW}) \sim 2.5$, which yields a value about 0.5 - 1 dex higher from the predictions of [Risaliti, Salvati & Marconi \(2011\)](#). While we understand that the sample in [Risaliti, Salvati & Marconi \(2011\)](#) can have BHs with higher mass and/or lower accretion rate, the second reason for the discrepancy is the use of the uniform/constant covering factor of 0.24, a value that is motivated by the study of broad lines and satisfies the BEL \mathcal{EW} s, as we have seen in Section 5. [Baskin & Laor \(2005\)](#) shows that this value for covering factor for [O III] 5007 Å line ranges between 0.02-0.2. If we account for this additional factor of 10 (drop in \mathcal{EW}), we reach a good agreement with the observed values reported in [Risaliti, Salvati & Marconi \(2011\)](#). That we rely on r_{max} to be 100 pc, or lower, is an indication, that we usually observe more compact NLRs. This initial analysis shows here, that there is scope of discerning the nature of NLRs (and also BLRs) if a rigorous, systematic analysis of the variations of the LOC parameters are conducted for NLRs, a study beyond the scope of this paper.

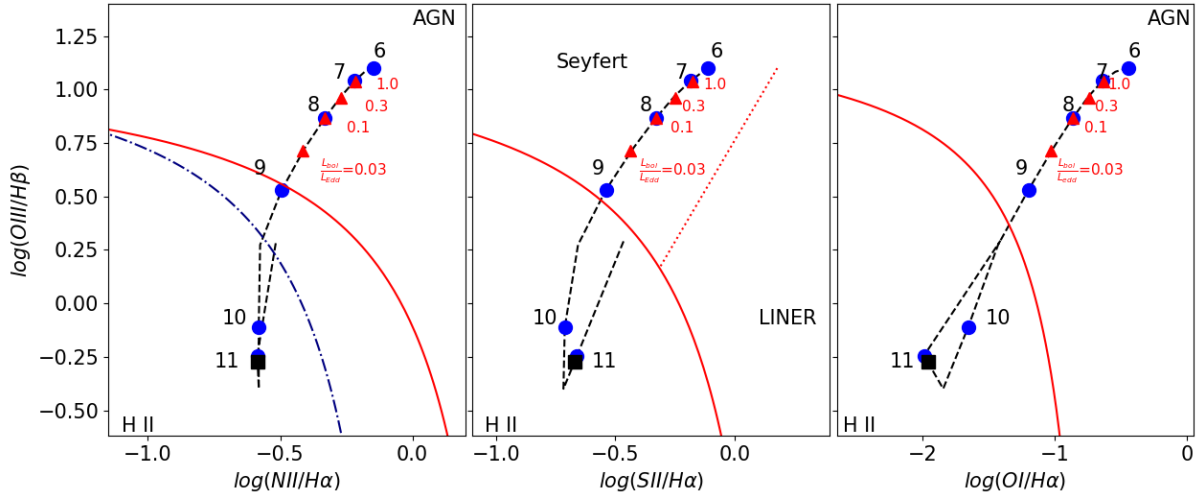


Figure 12. Line luminosity ratios of few observable prominent NELs as a function of BH mass for $L_{bol}/L_{Edd} = 0.1$ is plotted on Kewley et al. (2001 & 2006) plots (red line) and is marked in blue circles and are labeled with $\log(M_{BH}/M_{\odot})$ adjacent to them. Line luminosity ratios as a function of accretion rates, but only for $M_{BH} = 10^8 M_{\odot}$ is marked in red triangles. We have plotted a Black square corresponding to the AGN whose total luminosity is $10^{47} \text{ erg cm}^{-2} \text{ s}^{-1}$ to indicate the position of brightest known quasars on our plot.

7 LINE RATIOS

7.1 Narrow Lines and BPT diagrams

Unlike BELs, NELs are not direct signatures of AGN activity. For example, star-forming regions also emit Narrow (of the order of 100 km s^{-1}) emission lines. So, making the distinction between the two becomes very important. That is where the BPT diagrams become very useful. BPT diagrams were first plotted by Baldwin et al. (1981) to classify galaxies based on their excitation mechanisms. They found an empirical method of separating AGN from star-forming regions (SRFs) based on line ratios.

Kewley et al. (2001) used theoretical pure star photoionization models to give a maximum starburst line for some of the important BPT line ratios to distinguish AGN from SFRs more cleanly. We use the same line ratio planes as Kewley et al. (2001). The maximum starburst lines given by Kewley et al. (2001) are plotted as the solid red lines in each panel of the Figure 12.

The equations for these lines were as follows:

$$\log([O \text{ III}]/H\beta) > 0.61/[\log([N \text{ II}]/H\alpha) - 0.47] + 1.19 \quad (15)$$

$$\log([O \text{ III}]/H\beta) > 0.72/[\log([S \text{ II}]/H\alpha) - 0.32] + 1.30 \quad (16)$$

$$\log([O \text{ III}]/H\beta) > 0.73/[\log([O \text{ I}]/H\alpha) + 0.59] + 1.33 \quad (17)$$

There have been other schemes of demarcation as well. For example, the semi-empirical line given by Kauffmann et al. (2003) is marked as a dotted-and-dashed blue line in the left panel of Figure 12. As predicted by Kewley et al. (2001), the region below the solid red lines is expected to be the part of the plane populated by SFR line ratios, while the region above represents the AGN activity. As such, these line ratios have also become a method to look for AGN. Our theoretical predictions as a function of M_{BH} in the line ratio planes are traced by the dashed black lines in Figure 12, for $L_{bol}/L_{Edd} = 0.1$. We see that for the higher mass

black holes ($10^{8.5} M_{\odot} \lesssim M_{BH} \lesssim 10^{10.75} M_{\odot}$), the line ratios of NELs move into the star-forming regions of Kewley et al. (2001) plots. Hence these higher mass black holes will be incorrectly detected as SFR using these diagrams. We have further plotted the line luminosity ratios for different accretion rates L_{bol}/L_{Edd} (but only, for $M_{BH} = 10^8 M_{\odot}$) with red triangles in Figure 12. Note that, the less luminous BHs (even for lesser mass $\sim 10^8 M_{\odot}$) also start to seep into the SFR. This change is due to the disc SED being cooler, comparable to O-star temperatures, and so produce similar emission lines to H II regions. *Therefore, by using this method to distinguish AGNs from SFRs, we are losing low accretion rate and high mass black holes.*

7.2 Line Ratios for BELs

As seen in Figure 6, for some emission lines a particular $\log(\mathcal{EW})$ corresponds to two different BH masses. O VI 1034 Å, C IV 1549 Å and to some extent He II 1640 Å show degeneracy at the high mass end whereas Mg II 2798 Å, Hβ 4861 Å and Hα 6563 Å show degeneracy at the low mass end. Therefore, if we try to estimate the black hole mass using just the observed line strengths, we might end up with two very different values for BH masses agreeing to the observed line strengths. To remove this degeneracy we plot the line luminosity ratios on a multi-line plane as a counterpart to the BPT diagrams for NELs (Figure 13). Blue circles in the Figure 13 are line luminosity ratios for different masses for accretion rate $L_{bol}/L_{Edd} = 0.1$ traced by a black dashed line. The red triangles are line luminosity ratios for different accretion rates L_{bol}/L_{Edd} , but only for $M_{BH} = 10^8 M_{\odot}$. Such plots will be of use to determine the black hole mass just by using the observed line ratios. This may be a new tool for selecting HMBHs.

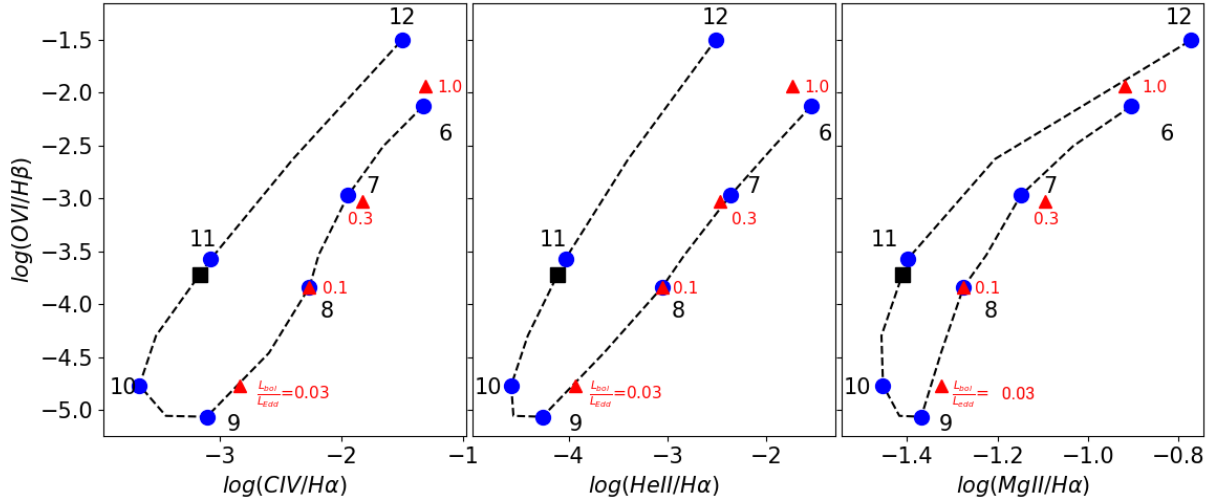


Figure 13. Line luminosity ratios of few observable prominent BELs as a function of BH mass for $L_{bol}/L_{Edd} = 0.1$ is marked in blue circles and are labeled with $\log(M_{BH}/M_{\odot})$ adjacent to them. Note that we use the line 1640 Å He II emission line in the middle panel, here, and in all subsequent figures of line ratios of BELs. We see that the degeneracy is lost when we plot the ratios on multi-line plane. Line luminosity ratios as a function of accretion rates, but only for $M_{BH} = 10^8 M_{\odot}$ is marked in red triangles. We have plotted a Black square corresponding to the AGN whose total luminosity is $10^{47} \text{ erg cm}^{-2} \text{ s}^{-1}$ to indicate the position of brightest known quasars on our plot.

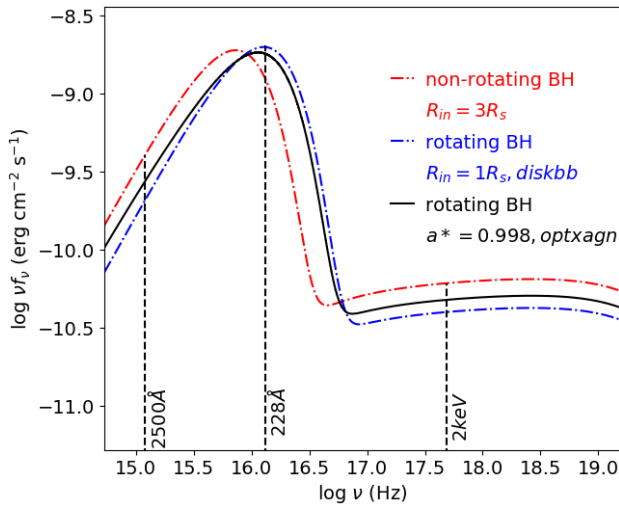


Figure 14. Comparison of SEDs of maximally spinning and non-spinning BH for $M_{BH} = 10^8 M_{\odot}$. Note that the peak of *diskbb* is more energetic and power-law component is less prominent for spinning BHs.

8 SPINNING BLACK HOLES

BHs are known to have spin associated with them (Reynolds 2014, 2019). Our analysis in the previous sections was motivated to look at the influence of mass variation on the changes in the line emission strengths. Just as the change in mass varies the SED, so does the variation in the spin of the BH (see Bertemes et al. (2016) for a detailed discussion). Hence, in this section, we look into the effect of the spin of the BHs. We do the same rigorous analysis of emission line strengths, as in previous sections, but comparing, only, the ‘maximally spinning’ BHs to the zero spin ones (analysed in the previous sections), because they will show the maximum deviation from the spin zero case. Results for any interme-

diate spin is beyond the scope of this paper - it is expected that results for the intermediate spin BHs will simply, lie in between. The more quantitative rigorous analysis will be conducted in future publications where we intend to compare theoretical predictions with observations.

Diskbb is a SED package that does not have spin as an explicit input parameter. However, since all SED generation in the previous sections relied on *diskbb*, we find a way to tweak and use the same package, for BHs with spin, for the sake of uniformity. We know that the innermost stable circular orbit of the accretion disc of a spinning black hole moves relatively closer (compared to that of a non-spinning or less spinning one) to the BH. Thus, in Equations 1 and 3, if we opt for a smaller value of R_{in} , while correctly adjusting for η , then we can mimic the SED of a spinning BH, even while using the package *diskbb*. To understand what will be a reasonable R_{in} modification to assume, we compare with an SED generated by the package *optxagn* (Done et al. 2012), from Xspec version 12.10. In *optxagn* we generated the accretion disc SED of a maximally spinning ($a^* = 0.998$) BH of mass $10^8 M_{\odot}$, accreting at $L_{disk} = 0.1 L_{edg}$. Keeping the mass and the accretion rate constant for the BH, when we used *diskbb* input parameters, we found a very good match of the SED, for $R_{in} = R_s = 2R_G$ (resulting in $\eta = 0.75$), while comparing $L_{\nu}(2500)$ and the energy where the SED peaks (two important aspects relevant to the analysis in this paper). Hence, we proceed to make this a norm for SEDs in this section (and the paper) for BHs with spin - we use *diskbb*, with R_{in} set to $R_s = 2R_G$. We understand that for a non-spinning black hole, $R_{in} = R_s$ (or $\eta = 0.75$) is less than the allowed limit of $3R_s$. Thus, for (*diskbb*), which is a package for spin zero BHs, using $R_{in} = R_s$ is unphysical - we made this choice as an artificial fix in the package which cannot include the effects of spin, in any other way. Figure 14 shows the comparisons of the resultant SEDs for $10^8 M_{\odot}$, accreting at $L_{bol} = 0.1 L_{edg}$ ($\theta = 30$ degrees). Compared to the Schwarzschild SED (red, dotted-and-dashed line), the peak

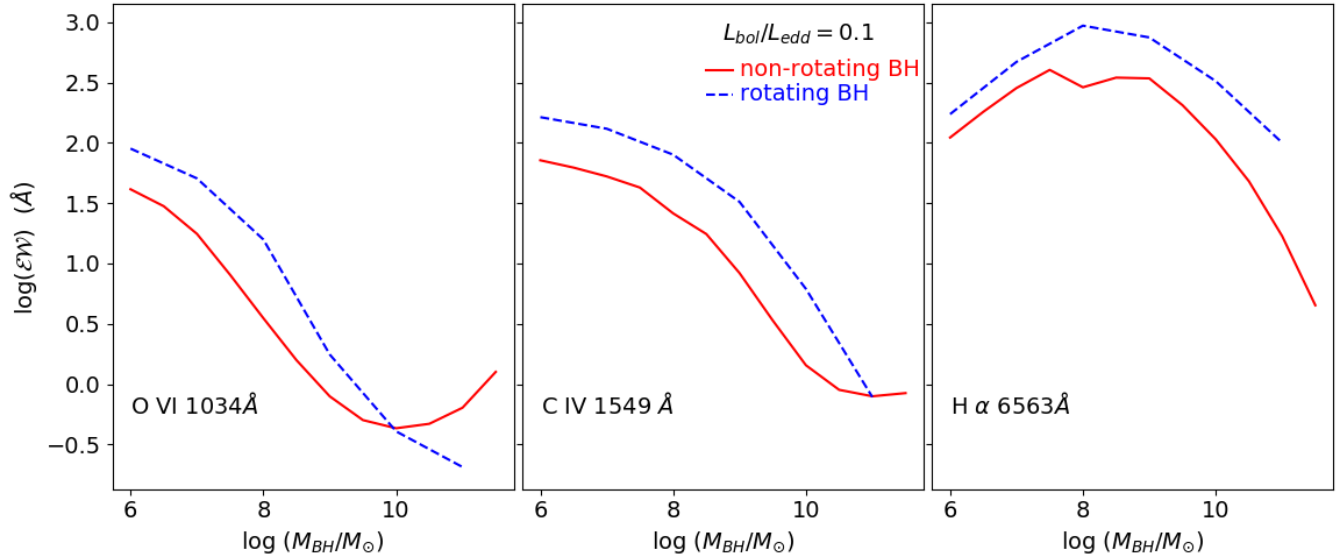


Figure 15. Evolution of some of the \mathcal{EW} as an extension from Figure 6. Even though the \mathcal{EW} of spinning BHs are stronger than the non-spinning BHs, the trend remains.

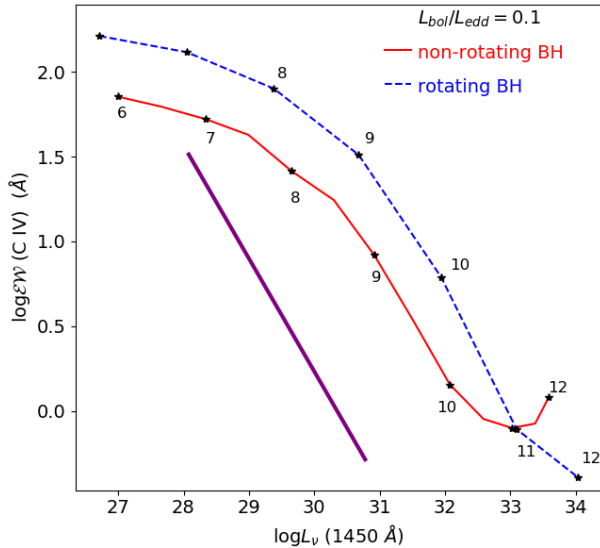


Figure 16. The Baldwin Effect demonstrated for the zero spin and highly spinning black hole.

of the SED for the maximally spinning BH is shifted by 0.25 dex (and 0.15 dex), higher in frequency, for the *diskbb* (and the *optxagn*) SED. At the HeII ionization edge (at 228 Å), the maximally spinning *diskbb* (and *optxagn*) SED is 0.2 dex (and 0.16 dex) higher in normalization than the Schwarzschild SED. We generate SEDs corresponding to a range of $10^6 \leq M_{BH} \leq 10^{11}$, but, this time, with an interval of 1.0 dex. These SEDs are then used through CLOUDY to predict emission line strengths for both BELs and NELs, in the same way that have been discussed in the previous sections, for the Schwarzschild BHs. The results of this analysis is presented in Figures 15 through 17.

We see that in the case of spinning BHs (of same mass $M_{BH} = 10^8 M_\odot$), \mathcal{EW} for C IV 1549 Å is higher (by 0.45 dex) than that for the Schwarzschild BHs and this factor decreases for HMBHs (Figure 15). However, the overall trend

of declining \mathcal{EW} , for all the lines, as a function of mass, still remains true even in the extreme case of maximum spin. We had noted earlier that for the O VI and C IV lines, the \mathcal{EW} turns over at the high mass end, for Schwarzschild BHs with $L_{bol}/L_{edd} \leq 0.1$. However, we do not see such turn-over for the spinning BHs. This is not surprising, because, for the same mass, the SED of the spinning BH has the same effect as the SED of BH with a higher accretion rate (see Figure 6). On the other hand, the \mathcal{EW} for H α drops much less, for spinning BHs!

Figure 16 demonstrates that the Baldwin effect, for the C IV line holds fort, for spinning BHs; in fact, higher the spin, better would be the match of the slope of the profile with the value $-2/3$ (-0.66), since the Baldwin effect is $\mathcal{EW} \sim L_\nu^{-2/3}(1450)$. For the non-spinning black hole, the slope is -0.53 for the mass range $10^8 - 10^{11} M_\odot$ and for the spinning black hole, the slope is -0.67 , for the mass range $10^9 - 10^{12}$.

Figure 17 shows the line ratios for the BELs (top panels) and NELs (bottom panels). There are clearly quantitative differences in the line ratios, but the overall trend remains the same even for the spinning BHs. Even though higher mass spinning BHs fall into H II region of Kewley plots, it happens only for $M_{BH} \geq 10^{10} M_\odot$ (as opposed to $M_{BH} \geq 10^9 M_\odot$ in the case of non-spinning BHs).

9 EMISSION LINE STRENGTHS IN LOWER MASS SCHWARZSCHILD BLACK HOLES

We have mainly focused in this paper on the super to hyper massive black holes, with the motivation to see how emission line strengths evolve as this transition is made. In Chakravorty et al. (2014), on the other hand, the authors had concentrated their efforts on the low mass black holes. Since, accretion disks of lower mass ($\leq 10^6 M_\odot$) peak at extreme ultraviolet, the part of the SED which ionises the line emitting gas, is entirely dominated by the disk SED. Hence, in Chakravorty et al. (2014) had ignored the power-law component. Reconstructing a disk plus power-law SED

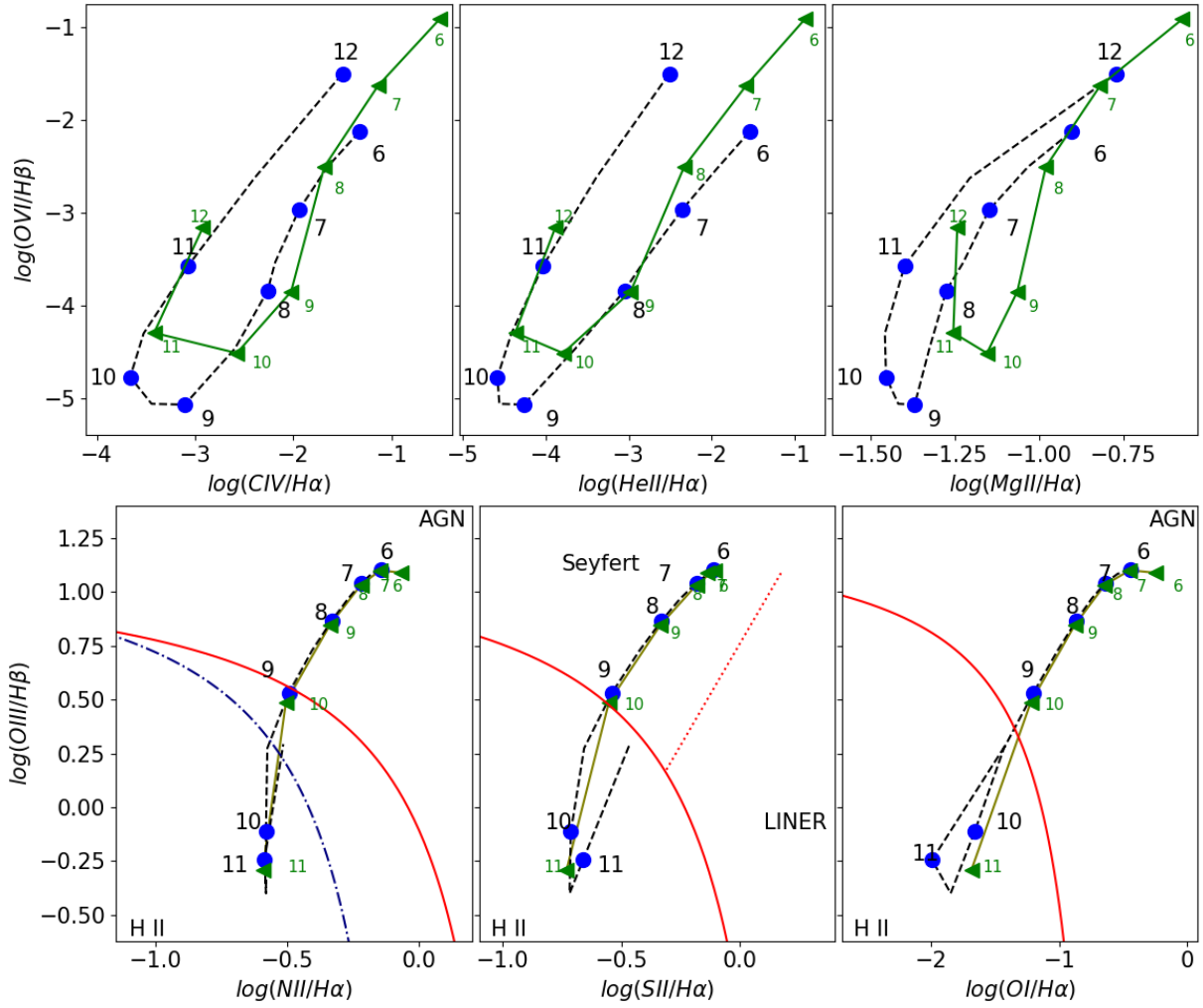


Figure 17. Extending Figures 13 and 12, we compare the broad (top panels) and narrow (bottom panels) emission line ratios of spinning BHs. Green triangles joined by the solid green line, in the figure, correspond to spinning BHs and are labeled with $\log(M_{BH}/M_{\odot})$ adjacent to them (smaller green fonts). For comparison, we retain the line ratio profiles for the non-spinning black holes through the black dashed curves joining the blue circles.

for the low mass black holes would require involved analysis of observations, and such an exercise is beyond the scope of this paper. However, following the cue of Chakravorty et al. (2014), we can rely on ‘approximate’ SEDs for the lower mass Schwarzschild black holes, where the disk is the only component. After construction of these SEDs, for $L_{bol}/L_{edd} = 0.1$, and $10^2 \leq M_{BH}/M_{\odot} \leq 10^5$ (at steps of 1.0 dex) we run them through CLOUDY to calculate the emission line strengths. Following the same methods, on the line emissions, as for the higher mass BHs, we try to build a ‘continuum’ of emission line properties across the entire mass range $10^2 \leq M_{BH}/M_{\odot} \leq 10^{12}$. While, the SEDs for the lower masses, may not be accurate, we get a few interesting insights.

Figure 18 shows that there is a ‘sweet spot’ in BH mass range $10^6 - 10^9 M_{\odot}$, where the strong emission lines like C IV and H α peak and their $\mathcal{E}W$ drop sharply, on both sides of this mass range! This is a striking result, because this gives us an insight into the resultant selection bias that all emission line surveys must have in favour of $10^6 - 10^9 M_{\odot}$ BHs. This is in fact where most AGN BH masses are found

(e.g. in Shen et al. 2011, and references therein). Given this bias, it could be that the true range of BH masses is much broader than has been supposed. O VI seems to have a constant strength down to masses, as low as $10^4 M_{\odot}$. So, in the search for intermediate mass BHs, this would be the best emission line to target. OVI is hard to detect, however, as it requires far UV spectroscopy at low redshifts, as from FUSE (Kris 2004), while at high redshifts it is almost always absorbed by the Lyman alpha forest.

Figure 19 shows the line ratios for the entire mass range, for BELs (top panels) and NELs (bottom panels). The BPT diagrams of the ratios of the different narrow emission lines is a common tool, now, not only to distinguish AGN from star forming regions but even to distinguish Seyfert-like AGN from LINER-like AGN. Note that Chakravorty et al. (2014) had presented some results about how the $\mathcal{E}W$ of broad emission lines will look like, albeit with much less rigour than has been used in this paper. However, there has been no investigation of the evolution of the BPT diagrams, concentrating on the low mass end. In Kewley et al. (2006), the authors had introduced a dividing line between Seyferts

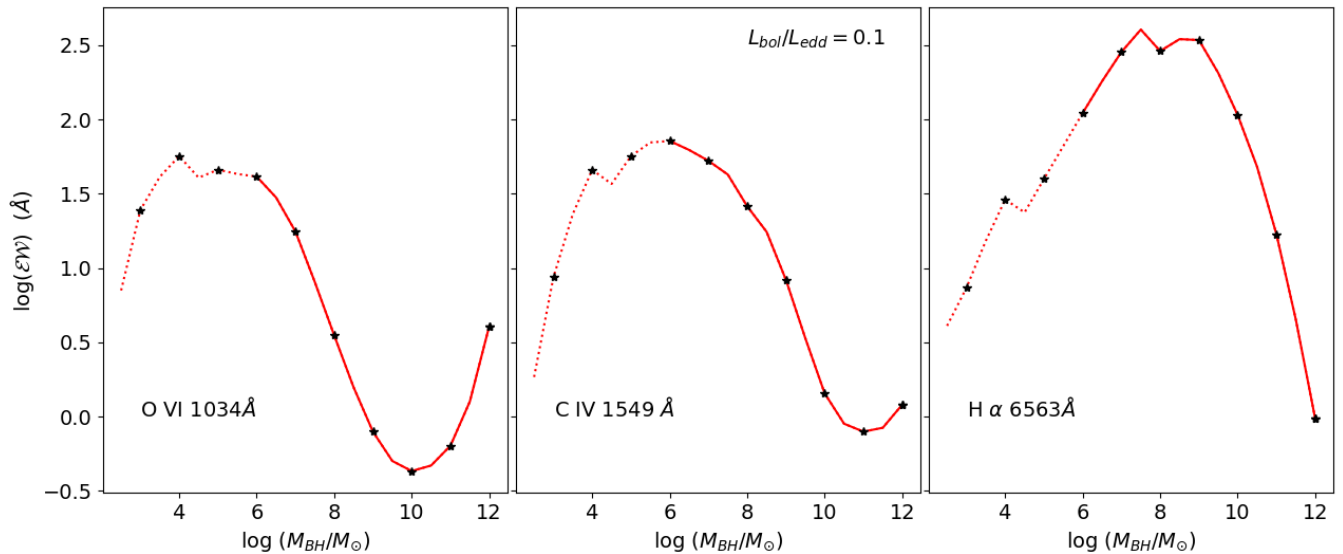


Figure 18. Evolution of some of the \mathcal{EW} as an extension from Figure 6. The \mathcal{EW} for the lower mass black holes (traced by red dotted lines joining the stars) are added to show the variation across the entire BH mass range.

and LINERS, shown as the dotted red line on the (middle) $\log([\text{O III}]/\text{H}\beta)$ vs $\log([\text{S II}]/\text{H}\alpha)$ and the (right) $\log([\text{O III}]/\text{H}\beta)$ vs $\log([\text{O I}]/\text{H}\alpha)$ line ratio planes. In Figure 19, bottom panels, while in the middle panel even the low mass BHs are consistent with Seyfert-like line ratios (except for $\log(M_{\text{BH}}/M_{\odot}) \lesssim 2$), in the right panel, BH with masses lower than $10^{4.5}M_{\odot}$ are consistent with being LINERS.

A more rigorous calculation about the low mass BH NELs is beyond the scope of this paper, because this paper deals with HMBHs.

10 DISCUSSION

10.1 On Truncated discs and Radiatively Inefficient Accretion flows

To model the radiation from the accretion disc, we have used the ‘thin disc paradigm’ and used the Shakura Sunyaev model (Shakura & Sunyaev 1973; Frank, King & Raine 2002) where $L \sim \dot{m}$, however, when the accretion rate decreases below $\dot{m} < 0.01$, $L \sim \dot{m}^2$. The accretion flow close to the BH becomes very different, the disc becomes optically thin and geometrically thick and radiatively inefficient. We are pursuing the calculations for such radiatively inefficient accretion flow (RIAF) in a separate analysis. In such cases, there are often signatures that the innermost parts of the accretion disc are truncated, where the radiatively inefficient flow dominates, and there is an outer thin disc. SEDs, corresponding to such scenarios are different flavours of the may be similar to the RIAF SEDs. We will address such SEDs, also, in the RIAF paper. Since these SEDs are predicted to be ‘dim’ in UV and optical but bright in X-rays, in addition to looking at the emission line properties, we will also look into the properties of the X-ray warm absorbers for SMBH harbouring RIAFs.

10.2 On the 150 eV soft excess component of AGN SEDs

X-ray observations from ROSAT and XMM-Newton show the presence of unaccounted excess intensity at $E < 1$ keV known as the *soft excess* component, in the observed spectra of type1 AGN. (Elvis, Wilkes & Tananbaum 1985; Brinkmann 1992; Buehler et al. 1995; Pounds & Reeves 2002). This component is usually by a blackbody with temperature $T_{\text{se}} \sim 100 - 200$ eV (i.e. peaking at $\sim 282 - 564$ eV) (Matsumoto, Leighly & Marshall 2004; Piconcelli et al. 2005; Porquet et al. 2004; Vignali et al. 2004, and references therein). The ratio of the *soft excess* luminosity to power-law luminosity (between 0.1 - 10 keV) is independent for each object, for e.g. it is 0.04 in Mkn 304 (Piconcelli et al. 2005) and $\gtrsim 1.0$ in Ark 564 (Vignali et al. 2004). The *diskbb* model, though represents UV SED of the observed AGN spectra satisfactorily, cannot model the *soft excess* component because centres of SMBHs are too cold to reach the peak temperature at ~ 0.5 keV. *soft excess* component can be explained only by making modifications to the *diskbb* model (Czerny & Elvis 1987; Korista, Ferland & Baldwin 1997) or by introducing an additional spectral component.

In this paper, we have ignored the *soft excess* as a component of the AGN SED. Because the physical origin of the *soft excess* component is not certain, hence it is not easy to relate it, in a systematic way, to either the accretion disc component or the power-law. There is no empirical relation that will guide us to find the evolution of the *soft excess* component as a function of the BH mass. The task of finding the correct prescription to relate these components is beyond the scope of this paper. In our future attempts at deriving more physically motivated SED, we can use (for example) optxagn to generate the *soft excess* as a function of the disc component (which will have a dependence on the mass of the BH).

The *soft excess* component could be further ignored, for this paper, because of the energy range where it dominates.

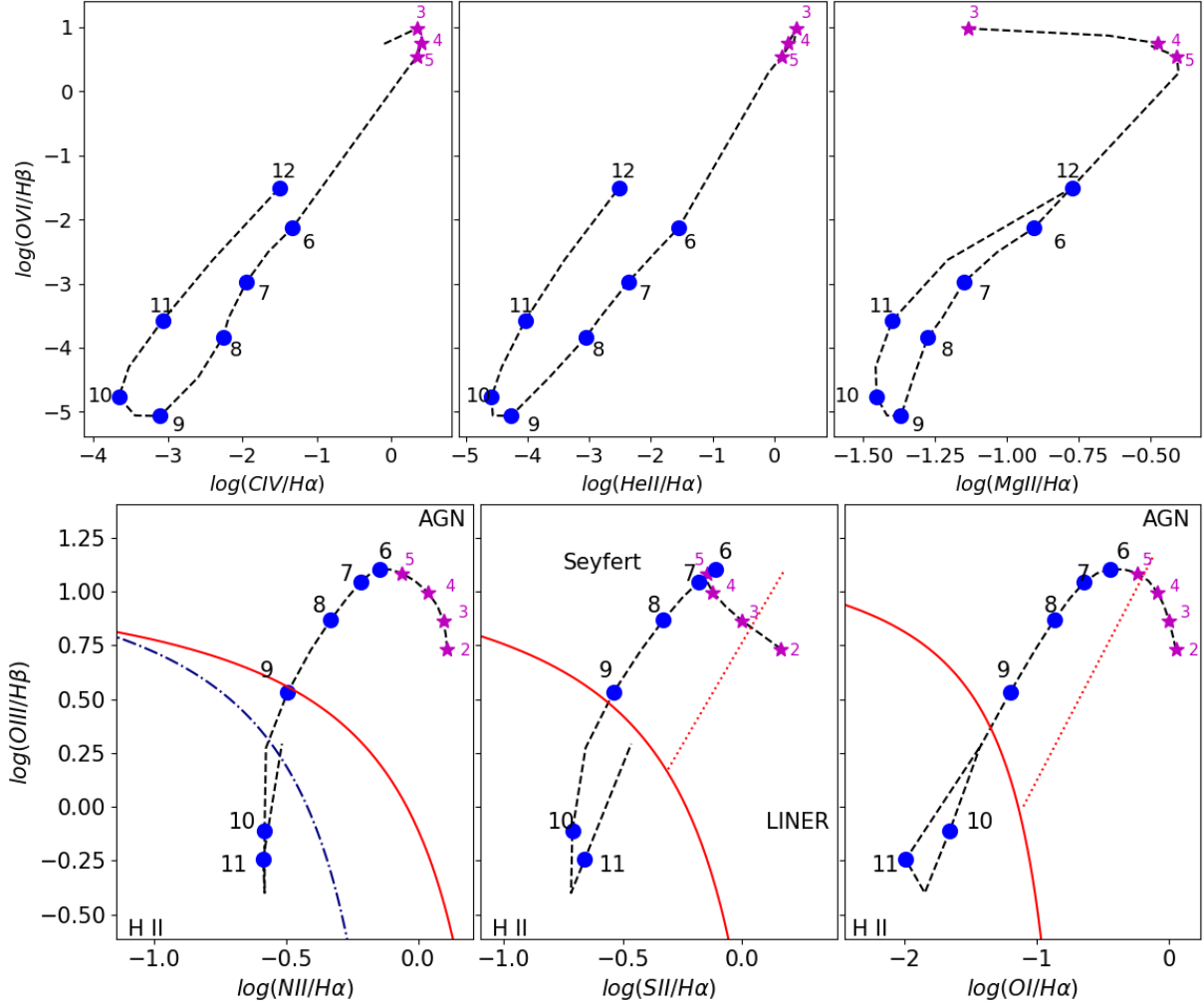


Figure 19. As an extension from Figure 12, we have calculated the line ratios for lower mass black holes, $10^2 M_\odot < M_{BH} < 10^6 M_\odot$ (extended black dashed line, studded with magenta star symbols) at a steps of 1 dex. We have used just the *diskbb* component of the SED.

As mentioned above, *soft excess* peaks at $\sim 282 - 564$ eV. The ions emitting the broad and narrow emission lines, discussed in this paper, are unlikely to be influenced by photons with such high energies - for example, the IP of O V is ~ 114 eV and the central wavelengths of all the lines are in the UV range. So, for the purpose of this paper, the *soft excess* would have been a redundant component.

11 CONCLUSIONS

- The motivation of this paper was to test, for Schwarzschild BHs, a) if there is a higher mass cut-off above which black holes cannot efficiently produce typical BELs such as O VI 1034 Å, C IV 1549 Å, He II 1640 Å, Mg II 2798 Å, H β 4861 Å and H α 6563 Å used to detect AGNs, b) how would ratios of the NELs evolve for the Hypermassive ($\gtrsim 10^9 M_\odot$) black holes, in the standard BPT diagrams involving H β 4861 Å, [O III] 5007 Å, [O I] 6300 Å, H α 6563 Å, [N II] 6584 Å and [S II] 6720 Å.

- We wanted to probe the Hypermassive Black Holes (HMBHs) with mass $\geq 10^8 M_\odot$. The first step in the analysis

was to build a method of producing systematic mass dependent AGN SEDs for the range $10^6 - 10^{12} M_\odot$. For HMBHs, the peak of the disc component moves to lower energies and hence the important conventional wavelength of 2500 Å sees a different part of the disc radiation in case of the most massive HMBHs. We used the latest empirical results known, for the Supermassive Black Holes and used judicious extrapolations to form a suite of SEDs for all BHs in the aforementioned mass range.

- These suites of SEDs were used in CLOUDY to calculate emission line strength for gas clouds with a wide range of densities and placed over a wide range of distance from the black hole. This exercise was done for both the (popularly known) broad and narrow emission lines. The CLOUDY calculated EWs of the individual clouds were then suitably added and averaged using the ‘Locally Optimally Emitting Cloud’ model to predict the final effective equivalent width \mathcal{EW} and luminosity of the emission lines. These emission line strengths and their ratios were then used to predict observables for the HMBHs.

- We found that the optical BELs, like H β 4861 Å and H α 6563 Å are not the best tracers to look for HMBHs because

these lines' \mathcal{EW} drop by about a factor of ~ 100 as mass increases from 10^8 to $10^{10} M_\odot$. This is a very important point to note because large optical surveys like SDSS use these optical broad lines to look for AGN activity. If we want to look for HMBHs, the ultraviolet line O VI 1034 Å would be the most useful because its strength undergoes a significant and interesting turnover, from their drop, in intensity, for the highest mass black holes.

- The Baldwin effect is clearly reproduced by the changing SEDs in our calculations. C IV \mathcal{EW} scales as $\sim L_\nu^{-2/3}(1450)$ for the super to hypermassive BHs ($\sim 10^8 - 10^{10} M_\odot$). It approximately holds for accretion rate, as low as 0.03, but the relationship matches better for higher accretion rate (or higher spin of the BH), and also spans a larger mass range (up to $\sim 10^{11} M_\odot$).

- Studying the BPT diagrams for the NELs, reveals that BHs with the highest mass with/or low accretion rate may have line ratios consistent with star-forming regions, thus making it very difficult to find them in this way. This, further, implies that the number of actively star-forming regions are being overestimated in large survey samples like SDSS and the number of massive black holes are being underestimated. This effect adds to the above-mentioned bias against HMBHs in broad line detection). Such a realisation should have a **profound** effect on the luminosity functions of both these classes of objects, namely AGN and normal (but actively star-forming) galaxies.

- Following the principles of BPT diagrams, we have proposed line ratio diagrams for the BELs, too. The $\log(\mathcal{EW})$ profile is often degenerate in mass, which can be broken, by using the line ratio plots for BELs. Note that above mentioned degeneracy is pronounced and noticeable because we are dealing with a much wider mass range here.

- After considering Mass and accretion rates as two main BH parameters which alter the SED of the accretion disc, we also paid attention to the spin of the BH. Since maximally spinning black holes will have the most different SEDs, compared to Schwarzschild ones, we compared these two, for the super to hyper massive BH mass range, while holding the accretion rate constant at 0.1. The effect of the spin turned out to be similar to the effect of the accretion rate, for the BH of same mass. Both of these parameters tend to increase the peak energy E_{max} where the SED has a maxima. The drastic fall off of the line \mathcal{EW} with increasing mass cannot be arrested, for even the spinning black holes, they also satisfy the Baldwin effect. The spinning HMBHs also plunge into the SFR region of the BPT diagram, only for relatively higher masses. Only, if we have a maximally spinning high accretion rate (~ 1.0), HMBHs, then they may be populating the AGN region of the BPT diagrams.

- We have further, investigated the change of \mathcal{EW} for lower masses ($\leq 10^6 M_\odot$). We find that the strong observable emission lines like the C IV and H α favour a mass range $10^6 - 10^9 M_\odot$ and drop off sharply, in \mathcal{EW} , on both sides of this mass range! This is a striking result, because this gives us an insight into the resultant selection bias that all emission line surveys must have in favour of $10^6 - 10^9 M_\odot$ BHs. This is in fact where most AGN BH masses are found. Given this bias, it could be that the true range of BH masses is much broader than has been supposed. O VI is the best emission line to look for intermediate mass BHs as it maintains a constant \mathcal{EW} down to $10^4 M_\odot$. The BPT diagrams

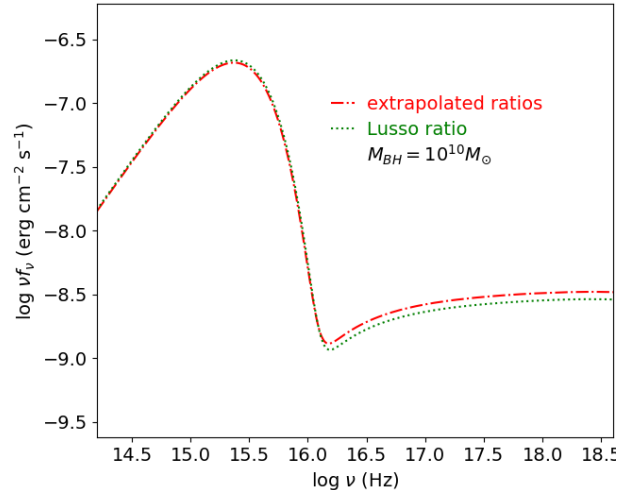


Figure A1. Comparison of SED (called ‘Lusso ratio’) constructed using “just” Eqn. 5 (Lusso & Risaliti (2016)) vs SED (called ‘extrapolated ratio’) using our more rigorous method using Figure 2 and Eqn. 6, for black hole of mass $10^{10} M_\odot$ and $L_{bol}/L_{edd} = 0.1$.

for lower masses show that for some line ratios, they tend to behave like LINERS.

- Our results show that weak emission lines from HMBHs would be very difficult to detect using the current optical facilities. However, these same results establish a benchmark which can be used by future 30 m class optical telescopes to look for HMBHs.

12 ACKNOWLEDGEMENTS

We thank the anonymous reviewer for useful comments and suggestions that helped us improve the quality of this manuscript significantly. HB acknowledges support from IISc, where a major fraction of this work was done during her project. SC was supported by the SERB National Postdoctoral Fellowship (File No.PDF/2017/000841). NR acknowledges support from the Infosys Foundation through the Infosys Young Investigator grant.

APPENDIX A: ADDING DISK AND POWER-LAW WITHOUT EXTRAPOLATION RELATION FOR HMBHS

In Section 2.3, we have described that to build our SEDs, we use a method of extrapolation to scale the L_{pl}/L_{disk} for HMBH, while using Equation 8 for the supermassive black holes. This is the method, which has been used throughout the paper and we call this method as ‘extrapolated ratio’ in this section. One might argue that Equation 8 does not distinguish between super and hyper massive black holes and so this equation should be used directly, even for the HMBHs and we should not be extrapolated. However, these extrapolations, which become important only for the HMBHs, are based on the physics of accretion discs. However, in this section, we show that if we directly used Equation 8 for the highest masses, to scale the power-law with respect to the

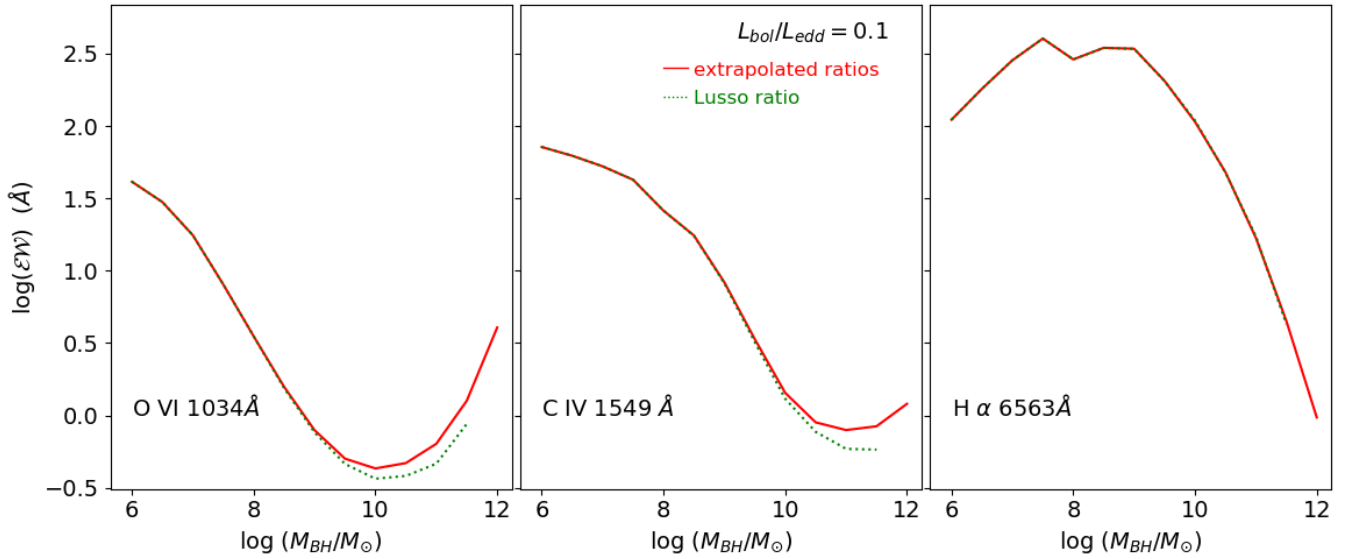


Figure A2. Comparison of some of the \mathcal{EW} as an extension from Figure 6. The SED generation schemes are marked in the Figure.

disk, and add the two components, the differences in the results would be minor, and effectively has no difference in the qualitative inferences. We call this second method of creating the SED (relevant in the context of the HMBHs, only) as ‘Lusso ratio’, in this section.

- In Figure A4, we show the SEDs of BHs of same mass $10^{10} M_{\odot}$ and $L_{bol}/L_{edd} = 0.1$, but different schemes of SED generation, as labeled. We demonstrate that the variation in SED is minor. Such SEDs were generated for $L_{bol}/L_{edd} = 0.1$, but only for BHs whose SEDs were generated using ‘extrapolated ratio’ method, namely the mass range $> 10^{8.25} M_{\odot}$. Note that BHs with lower mass, the ‘Lusso ratio’ method was anyway, used. So whatever differences arise because of the variation of scheme of SED creation, will affect the results for only the higher mass BHs.

- Referring to Figures A2 and A3 we see that there is absolutely no qualitative difference to the results.

REFERENCES

- Arnaud K. A., 1996, in Jacoby G. H., Barnes J., eds, ASP Conf. Ser. Vol. 101, Astronomical Data Analysis Software and Systems V. Astron. Soc. Pac., San Francisco, p. 17
- Baldwin, J. A., 1977, ApJ, 214, 679
- Baldwin, J. A. 1997, in ASP Conf. Ser. 113, IAU Coll. 159: Emission Lines in Active Galaxies: New Methods and Techniques, ed. B. M. Peterson, F.-Z. Cheng, & A. S. Wilson (San Francisco, CA: ASP), 80
- Baldwin J. A., Phillips M. M., Terlevich R., 1981, PASP, 93, 5
- Baldwin J., Ferland G., Korista K., Verner D., 1995, ApJ, 455, L119
- Baskin A., Laor A., 2005, MNRAS, 358, 1043
- Beloborodov A. M., 1999, in Poutanen J., Svensson R., eds, ASP Conf. Ser. Vol. 161, High Energy Processes in Accreting Black Holes. Astron. Soc. Pac., San Francisco, p. 295
- Bertemes C., Trakhtenbrot B., Schawinski K., Done C., Elvis M., 2016, MNRAS, 463, 4041
- Brightman M. et al., 2013, MNRAS, 433, 2485
- Brinkmann, W. 1992, in X-ray Emission from Active Galactic Nuclei and the Cosmic X-ray Background, ed. W. Brinkmann, & J. Truemper, MPE report 235, 143
- Buehler P., Courvoisier T. J. L., Staubert R., Brunner H., Lamer G., 1995, A&A, 295, 309
- Chakravorty S., Elvis M., Ferland G., 2014, MNRAS, 437, 740
- Coppi P. S., 1992, MNRAS, 258, 657
- Coppi P. S., 1999, ASPC, in Poutanen J., Svensson R., eds, ASP Conf. Ser. Vol. 161, High Energy Processes in Accreting Black Holes. Astron. Soc. Pac., San Francisco, p. 375
- Czerny B., Elvis M., 1987, ApJ, 321, 305
- Done C., Davis S. W., Jin C., Blaes O., Ward M., 2012, MNRAS, 420, 1848
- Elvis M., Wilkes B. J., Tananbaum H., 1985, ApJ, 292, 357
- Fan, X. et al., 2001, AJ, 122, 2833
- Ferguson J. W., Korista K. T., Baldwin J. A., Ferland G. J., 1997, ApJ, 487, 122
- Ferland G. J. et al., 2017, Rev. Mex. Astron. Astrofis., 53, 385
- Frank J., King A., Raine D.J., 2002, Accretion Power in Astrophysics, 3rd edn. Cambridge Univ. Press, Cambridge
- Gierlinski, M., Zdziarski, A. A., Poutanen, J., Coppi, P. S., Ebisawa, K., & Johnson, W. N. 1999, MNRAS, 309, 496
- Haardt F., Maraschi L., 1993, ApJ, 413, 507
- Hamann F., Korista K. T., Ferland G. J., Warner C., Baldwin J., 2002, ApJ, 564, 592
- Ichikawa K., Inayoshi K., 2017, ApJ, 840, L9
- Johnson J. L., Whalen D. J., Fryer C. L., Li H., 2012, ApJ, 750, 66
- Kauffmann G. et al., 2003, MNRAS, 346, 1055
- Kewley L. J., Dopita M. A., Sutherland R. S., Heisler C. A., Trevena J., 2001, ApJ, 556, 121
- Kewley L. J., Groves B., Kauffmann G., Heckman T., 2006, MNRAS, 372, 961
- King A., 2015, Proc. TORUS2015, University of Southampton, Winchester 14-17 September 2016, P. Gandhi and S.F. Hoenig
- Korista K., Baldwin J., Ferland G., Verner D., 1997a, ApJ, 108, 401
- Korista K., Ferland G., Baldwin J., 1997b, ApJ, 487, 555
- Korista K., Goad M.R., 2000, ApJ, 536, 284
- Kriss, G. A., 2004, astro.ph.11380K
- Kwan J., Krolik J. H., 1981, ApJ, 250, 478
- Laor A., and Davis S. W., 2011, MNRAS, 417, 681L
- Latif M. A., Ferrara A., 2016, PASA, 33, 51
- Leighly, K., & Casebeer, D. 2007, in ASP Conf. Ser. 373, The

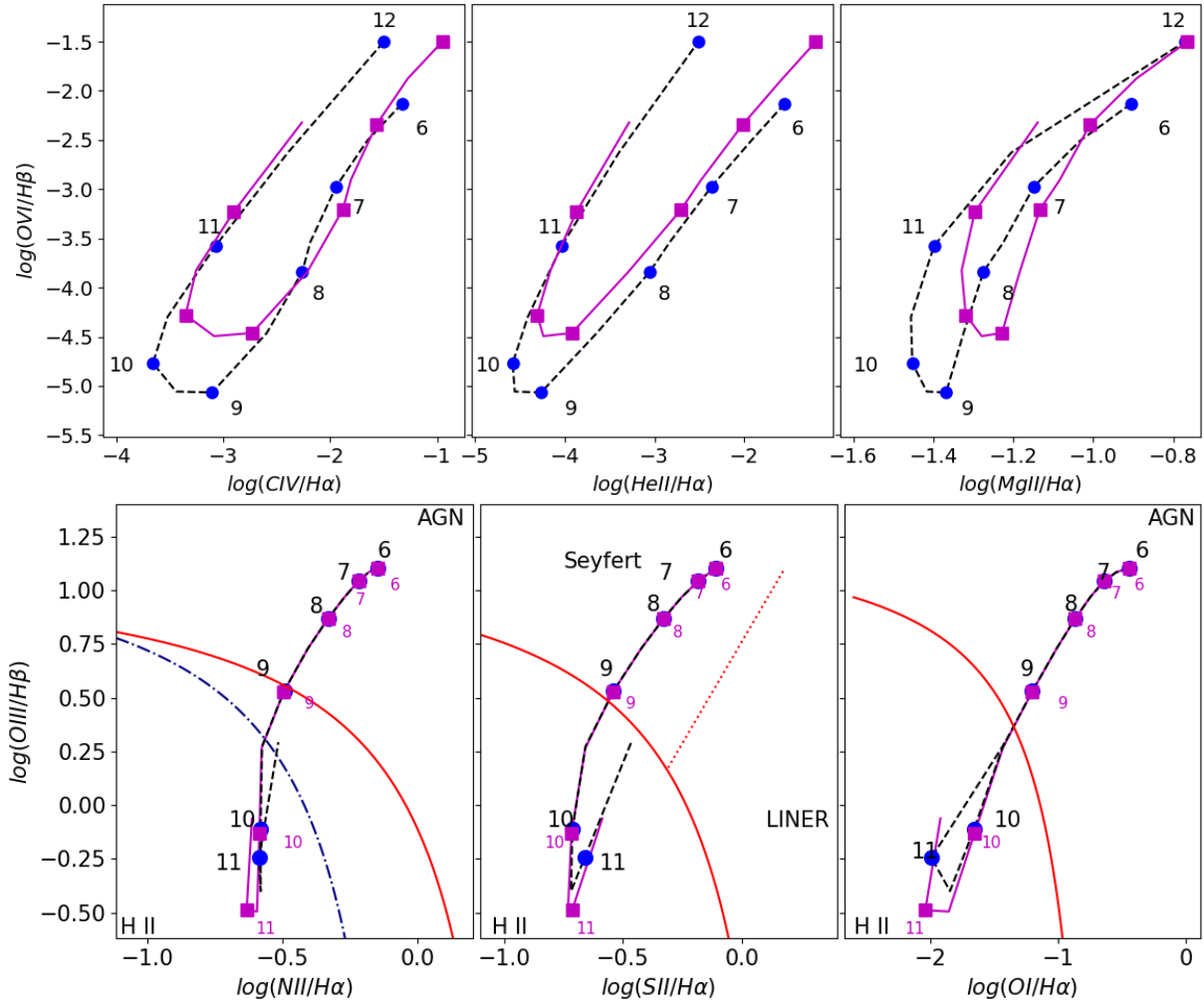


Figure A3. As an extension from Figures 12 and 13, we have calculated the line ratios for BELs (top panels) and NELs (bottom panels), to show the comparison of effects of SEDs, in Figure A1, but for all the higher masses, for $L_{\text{bol}}/L_{\text{edd}} = 0.1$. The solid magenta curves represent the results of the ‘Lusso ratio’ method.

Central Engine of Active Galactic Nuclei, ed. L. Ho, & J.-M. Wang (San Francisco, CA:ASP), 365
 Lightman A. P., Zdziarski A. A., 1987, pJ, 319, 643
 Lusso E., Risaliti G., 2016, 819, 154
 Lu Y., Yu Q., 1999, ApJ, 526, L5
 Makishima K., Maejima Y., Mitsuda K., Bradt H. V., Remillard R. A., Tuohy I. R., Hoshi R., Nakagawa M., 1986, ApJ, 308, 635
 Matsumoto C., Leighly K. M., Marshall H. L., 2004, ApJ, 603, 456
 Mitsuda K. et al., 1984, PASJ, 36, 741
 Mortlock D.J., 2011, Nature, 474, 616
 Natarajan P., 2014, GREGr, 46, 1702
 Natarajan P., Treister E., 2009, MNRAS, 393, 838
 Netzer H., 2015, ARA&A, 53, 365
 Netzer H., Laor A., Gondhalekar P. M., 1992, MNRAS, 254, 15
 Astrophysics of gaseous nebulae and active galactic nuclei, 2nd. ed. by D.E. Osterbrock and G.J. Ferland. Sausalito, CA: University Science Books, 2006
 Peterson B. M., 1997, An Introduction to Active Galactic Nuclei, Cambridge Univ. Press, Cambridge
 Piconcelli E., Guainazzi M., Cappi M., Jimenez-Bailon E., Scharrel N., 2005, A&A, 432, 835
 Porquet D., Reeves J. N., O’Brien P., Brinkmann W., 2004, A&A,

422, 85
 Pounds K., Reeves J., 2002, [arXiv:astro-ph/0201436]
 Reynolds C. S., 2014, Space Sci. Rev., 183, 277
 Reynolds C. S., 2019, NatAs, 3, 41
 Risaliti, G.; Salvati, M.; Marconi, A., 2011, MNRAS, 411, 2223
 Shakura N. I., Sunyaev R. A., 1973, A&A, 24, 337
 Shemmer O., Brandt W. N., Netzer H., Maiolino R., Kaspi S., 2006, ApJ, 646, L29
 Shemmer O., Lieber S., 2015, ApJ, 805, 124
 Shen, Y., 2011, ApJS, 194, 45
 Tananbaum H. et al., 1979, ApJ, 234, L9
 Trakhtenbrot B. et al., 2017, MNRAS, 470, 800
 Vignali C., Brandt W. N., Boller Th., Fabian A. C., Vaughan S., 2004, MNRAS, 347, 854
 Volonteri M., 2012, Science, 337, 544
 Wang J.-M., Watarai K.-Y., Mineshige S., 2004, ApJ, 607, L107
 Wu X.-B. et al., 2015, Nature, 518, 512
 Zdziarski A. A., Johnson W. N., Magdziarz P., 1996, MNRAS, 283, 193
 Zheng, W.; Malkan, M. A., 1993, ApJ, 415, 517
 Zimmerman E. R., Naraya R., McClintock J. E., Miller J. M., ApJ, 618, 832
 Życki P. T., Done C., Smith D. A., 1999, MNRAS, 309, 561